Molecular Electronic Transducer Based Seismic Motion Sensors

Micro-Fabrication, Packaging and Validation

by

Mengbing Liang

A Dissertation Presented in Partial Fulfillment
of the Requirements for the Degree
Doctor of Philosophy

Approved October 2016 by the
Graduate Supervisory Committee:

Hongyu Yu, Chair
Lenore Dai
Michael Kozicki
Hanqing Jiang

ARIZONA STATE UNIVERSITY

December 2016

ABSTRACT

The instrumentational measurement of seismic motion is important for a wide range of research fields and applications, such as seismology, geology, physics, civil engineering and harsh environment exploration. This report presents series approaches to develop Micro-Electro-Mechanical System (MEMS) enhanced inertial motion sensors including accelerometers, seismometers and inclinometers based on Molecular Electronic Transducers (MET) techniques.

Seismometers based on MET technology are attractive for planetary applications due to their high sensitivity, low noise floor, small size, absence of fragile mechanical moving parts and independence on the direction of sensitivity axis. By using MEMS techniques, a micro MET seismometer is developed with inter-electrode spacing close to 5 μm. The employment of MEMS improves the sensitivity of fabricated device to above 2500 V/(m/s^2) under operating bias of 300 mV and input velocity of 8.4μm/s from 0.08Hz to 80Hz. The lowered hydrodynamic resistance by increasing the number of channels improves the self-noise to -135 dB equivalent to 18nG/ √ Hz (G=9.8m/s^2) around 1.2 Hz.

Inspired by the advantages of combining MET and MEMS technologies on the development of seismometer, a feasibility study of development of a low frequency accelerometer utilizing MET technology with post-CMOS-compatible fabrication processes is performed. In the fabricated accelerometer, the complicated fabrication of mass-spring system in solid-state MEMS accelerometer is replaced with a much simpler post-CMOS-compatible process containing only deposition of a four-electrode MET structure on a planar substrate, and a liquid inertia mass of an electrolyte droplet. With a

specific design of 3D printing based package and replace water based iodide solution by room temperature ionic liquid based electrolyte, the sensitivity relative to the ground motion can reach 103.69V/g, with the resolution of 5.25μG/ √ Hz at 1Hz.

By combining MET techniques and Zn-Cu electrochemical cell (Galvanic cell), this letter demonstrates a passive motion sensor powered by self-electrochemistry energy, named “Battery Accelerometer". The experimental results indicated the peak sensitivity of battery accelerometer at its resonant frequency 18Hz is 10.4V/G with the resolution of 1.71 μG without power consumption.

DEDICATION

To Mom and Dad

the doctors who save lives and souls

To Mei

My love for you shall live forever

ACKNOWLEDGMENTS

I would like to express my special appreciation and thanks to my advisor Professor Dr. Hongyu Yu, you have been an outstanding mentor for me in both academic and career coach. I would also like to thank my committee members, Professor Michael Kozicki, Lenore Dai, Hanqing Jiang for serving as my committee members even at hardship.

A special thank for all my colleagues at ASU, Hai Huang, Rui Tang, Ruirui Han, Zuofeng Zhao, Yiwei Wang, Teng Ma, Zeming Song, Shule Yu, Sihan Zhang, Dongmin Han, Stella Nickerson, Evan Chen, Shiyan Zhu, Xu Wang, Wenhao Chen and Cheng Lv.

I would specially thank to Prof. Vadim Agavonov and NASA PIDDP0NNX10AL25G (USA) project.

TABLE OF CONTENTS

Page

LIST OF TABLES

LIST OF FIGURES

Figure Page

CHAPTER 1

BACKGROUND OF SEISMIC INSTRUMENTATION

In this chapter, I will introduce the history of the development of seismic instruments and the basic concept of seismology and its applications. The history of seismic instruments includes examples of ancient seismiscopes, modern seismographs and traditional and MEMS state-of-art seismometers. Besides the earthquake early-warning, the academic applications of seismometers including the study of earthquake, planetary exploration and ocean exploration will be discussed in the chapter.

History of Seismometers

The developments of seismic motion instruments can be divided into three periods in history: seismoscope, seismograph, seismometers. The seismiscope could only indicate the occurred great earthquake with its direction. The seismopgrah could record the time and amplitude of seismic movement mechanically with high resolution. Seismometers replaced the mechanical recording system with electrical data acquisition which were benefited from the development of analog and digital circuits.

Seismoscope

There were many of seismic motion records during our human's long history. The ancient people believed, an earthquake was caused by God's acts or some supernatural powers, which brought disasters, as punishment for misbehavior. Although modern scientific investigations of earthquakes began in the 1880s [1], which was benefited from the development of modern seismometry, the technical discipline with detection and measurement of seismic ground motion, the first seismic instrument in terms of today seismoscope was invented in AD 132 by Chinese Chang Heng as shown in Figure 1. [2]

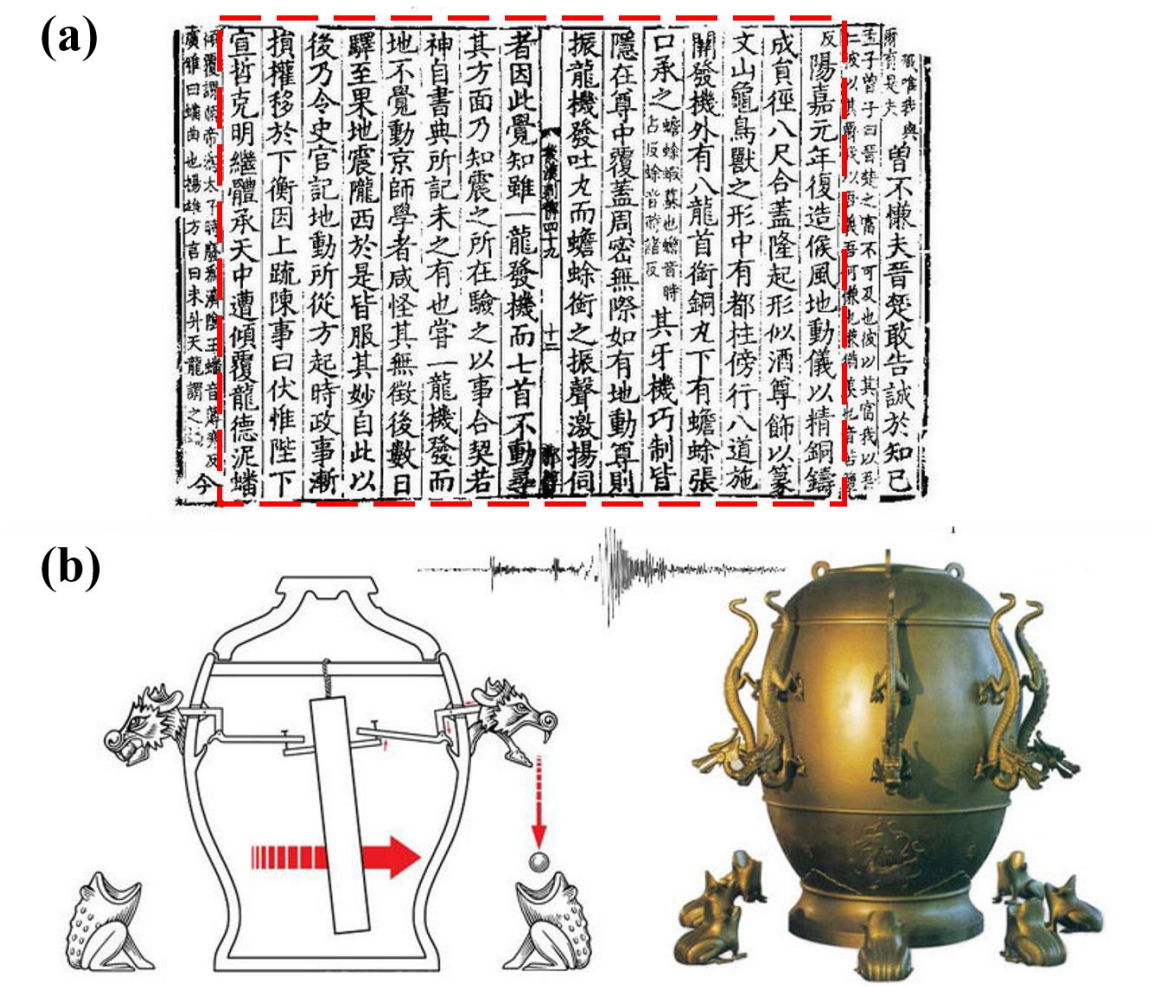

Figure 1. Ancient Seismoscope in China by Chang Heng. (a) Literature record of the function of Di Dong Yi. (b) The photo of rebuild Di Dong Yi.

According to the ancient literature, this instrument was designed to indicate the occurrence of an earthquake and its direction. Its appearance looks like a jar decorated with 8 dragons surrounded by 8 chi (mythical creatures similar to frogs). There is a ball in each dragon's mouth. With a pillar as inertial mass connected with eight transmitting rods to the dragons' mouths, the seismic wave by an earthquake will cause a movement of the inertial pillar which will transmit the force to the ball in the direction of earthquake center. The ball will then drop off into the chi's mouth which causes a ring sound. Each earthquake

only made one ball drop. The record showed that, there was one time the dragon spilled one ball but no earthquake was felt in that direction. Several days later, news came that there were an earthquake hundred miles away, which was a prove of its sensitivity.

A similar but liquid based seismoscope shown in Figure 2 was introduced in 1703 by J. de la Haute Feuille in Europe. It consisted a central reservoir filled with mercury and cups around the periphery. Weak vibrations especially the S-wave will cause spilling of liquid mercury into cups in the earthquake direction. [3]

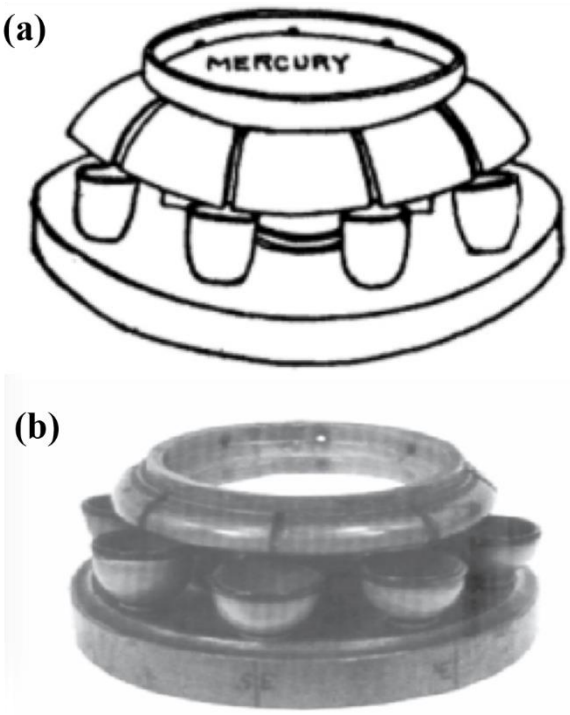

Figure 2. J. de la Haute Feuille's seismoscope (a) schematic the mercury seismoscope (b) the photo of mercury seismoscope

In 1855 Italy, Luigi Palmieri invented a more complex seismoscope with higher resolution based on solid-mass-spring system shown in Figure 3. [3] The mechanical parts included a pendulum inertial mass suspended by a spiral spring and complex mechanical

connections to amplify the inertial motion. A clock and a simple circuit were connected to the mechanical system to indicate the time when earthquake happened.

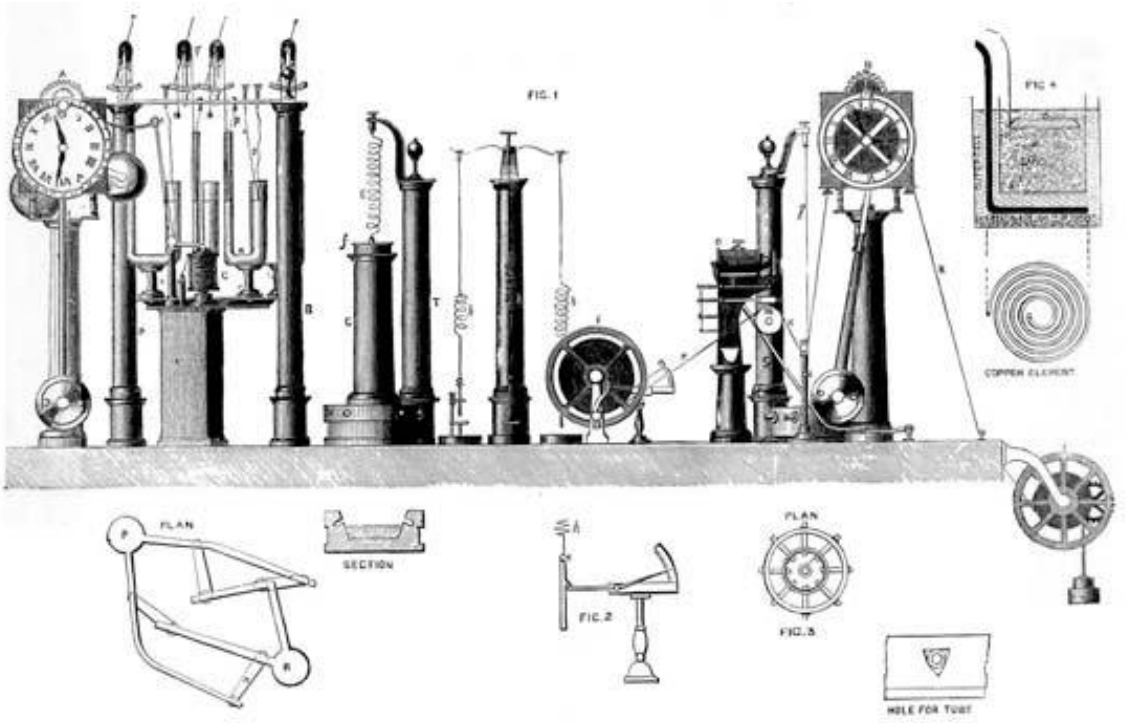

Figure 3 The Eruption of Vesuvius in 1872 by Luigi Palmieri (Asher and Company, London, 1873)

Seismograph

20 years later after Luigi's seismescope, Filippo Cecchi developed a two axis seismograph shown in Figure 4 (a) which could not only record the time, but also the amplitude of seismic movements. [3] The magnification of this equipment was very limited, so it could not record any but the strong shocks on the ground. Filippo's device included a pendulum which could move both south-north and west-east horizontally and a pen was connected under the inertial mass.

In 1876 Japan, English seismologist John Milne associated with Thomas Gray and J. Alfred Ewing developed a practical seismograph which influenced the seismology very much as shown in Figure 4 (b). An inertial mass was suspended below a boom which was connected to the top of a pivot's top. A photosensitive paper was provided to record the seismic wave. [4]

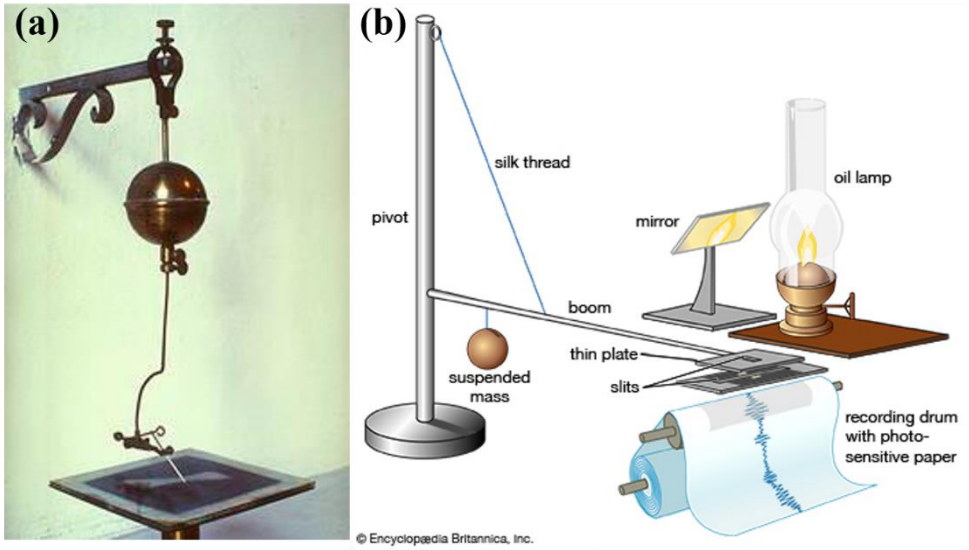

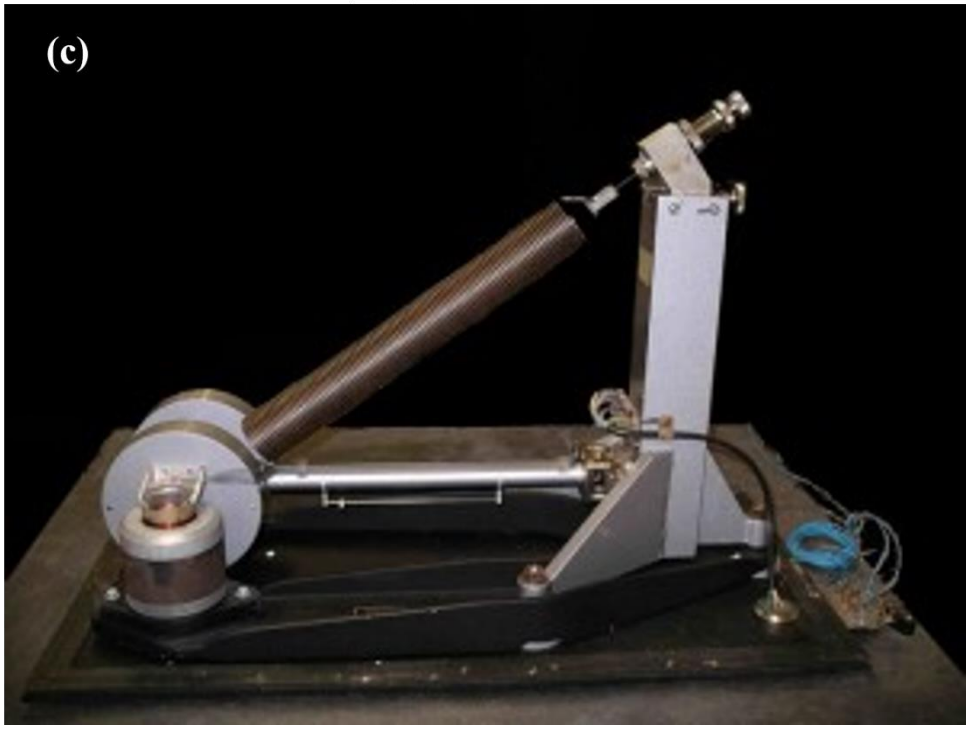

Figure 4 Ninety century seismograph (a) Cecchi brief period seismograph, Ximenes Observatory, Florence. (b) John Milne's seismograph, by encyclopedia Britannica, Inc. (c) Press-Ewing/Sprengnether seismograph. (Royal Observatory of Belgium)

In 1899, Ewing improved Milne's instrument shown in the Figure 4 (c). [5] The inertial mass was mounted on bracket and supported by two spring. A scriber was employed as an arm providing amplification of ground movement. The resolution of the whole system was improved by six times. It had extremely low resonant frequency profit from the large mass and elastic spring design, which allows unprecedented resolution in measuring seismic vibrations. Until ninety centuries, seismology was only limited in study of great earthquake. Profit from the improvement of seismograph, seismologist began to study in the seismic waves caused by the propagation in the earth.

Seismometer

In 1898, Emil Wiechert first time introduced dashpots into seismograph systems, which performed as a feedback force to balance the restoring forces. The working bandwidth of spring-mass system was dramatically improved. In 1903, B.B. Galtizen developed an electromagnetic seismometer. It was the first time an instrument can convert weak ground movements into electrical signals. In 1950s after World War II, electronic technology's bloomy evolution provided a well-developed electronic data acquisition system in application of seismometers. Dr. Benioff Horizontal graduated from Cal-Tech, United States successfully developed a modern seismometer including mass-damped-spring system, electromagnetic system and an electrical data acquisition system shown in

Figure 5. The global seismic institutions were then built up and the modern seismology was set up. [6]

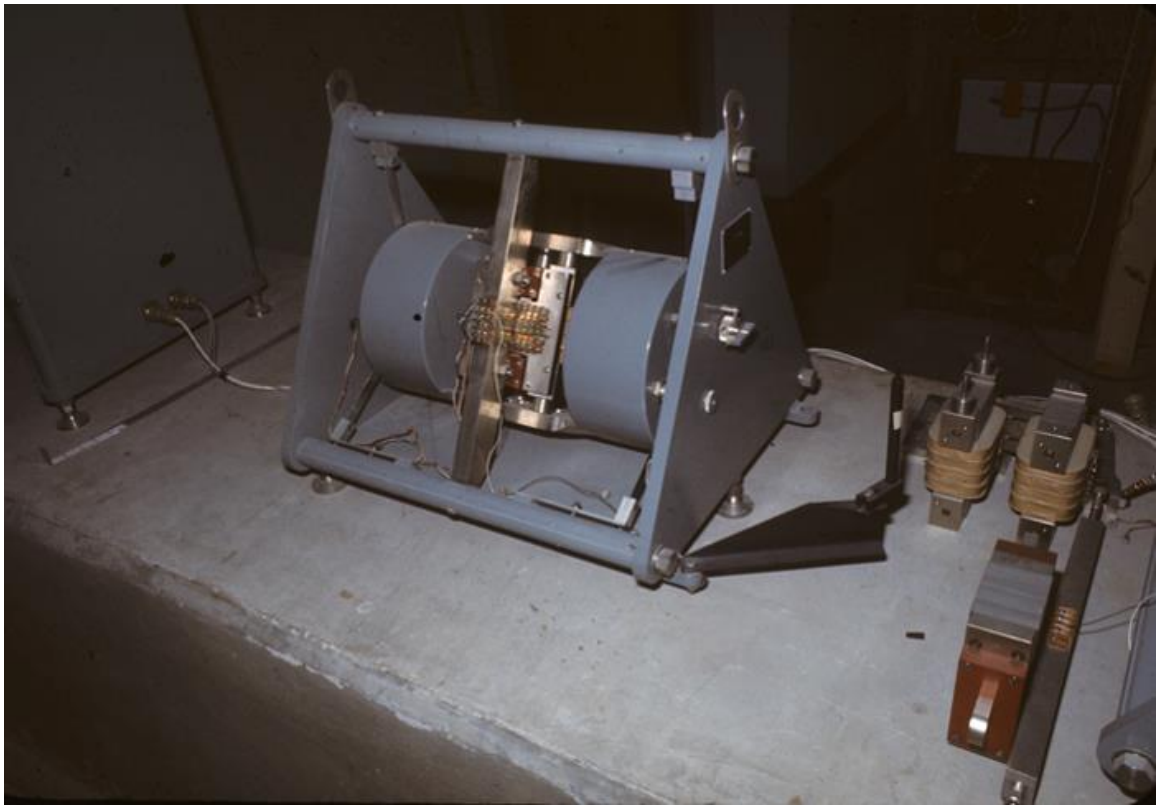

Figure 5 Dr. Benioff Horizontal's seismometer with electronic recording system, NOAA's Historic Coast & Geodetic Survey (C&GS) Collection

Earthquake study

The most common explanation of earthquake from ancient and medieval people was similar to any other natural disaster, which was caused by an act of God or other supernatural power. The scientific discussion firstly appeared in 18th century. The expansion of professional science in earthquake studies started in 19th century, which mainly about the connections between the astrology and earthquake occurrence. With the development of ongoing unfelt small motion sensors, the seismology which was also named as "endogenous meteorology" was born in 1880s. With the foundation of World-Wide Standard Seismograph Network (WWSSN) in 1950s, the modern era of seismology brought a series of impressive developments such as, studies of earthquake, underwater exploration and space exploration. [6]

Studies of Earthquake

Earthquake as one of the destructive disasters, causes potentially large total losses due to damage to buildings, infrastructure and lost economic activity. According to the report from U.S. Federal Emergency Management Agency (FEMA), Table 1 indicates the top 20 annual earthquake loss (AEL) cities in United States in unit of million dollars. [7]

Rank	City	State	AEL (million $)
1	Los Angeles-Long Beach-Santa Ana	CA	1,312.3
2	San Francisco-Oakland-Fremont	CA	781.0
3	Riverside-San Bernardino-Ontario	CA	396.0
4	San Jose-Sunnyvale-Santa Clara	CA	276.7
5	Seattle-Tacoma-Bellevue	WA	243.9
6	San Diego-Carlsbad-San Marcos	CA	155.2
7	Portland-Vancouver-Beaverton	OR	137.1
8	Oxnard-Thousand Oaks-Ventura	CA	111.0
9	Santa Rosa-Petaluma	CA	68.6
10	St. Louis	MO-IL	58.5
11	Salt Lake City	UT	52.3
12	Sacramento-Arden-Arcade--Roseville	CA	52.0

13	Vallejo-Fairfield	CA	39.8
14	Memphis	TN	38.2
15	Santa Cruz-Watsonville	CA	36.2
16	Anchorage	AK	34.8
17	Santa Barbara-Santa Maria-Goleta	CA	34.4
18	Las Vegas-Paradise	NV	33.1
19	Honolulu	HI	32.0
20	Bakersfield	CA	30.0

Table 1. Top 20 Areas of Annual Earthquake Loss (AEL) in United States (2014)

The old measurement of earthquake size is to indicate the earthquake intensity, which was a description of the effects, such as the observed damage, public's reactions and the environment changes, at that location. Nowadays, the global seismic networks are developed for the study of weak seismic waves and great earthquakes. The ability to study and localize the earthquake immediately needs two basic requirement of instrumentation, which are the recording of accurate time and determining the frequency dependent amplitude. The most popular method to scale the size of earthquake was provided by Charles Richter in 1934. [8] The Richter scale introduced a formula based on amplitude of the largest recorded seismic wave on seismometers and the distance between the earthquake and the instrument. Based on U.S. Geological Survey documents, Table 2 describes the typical effects of different levels of earthquake and its frequency of occurrence. [9]

Magnitude	Class	Effects	# per year	Acceleration (g)
2.5 or less	Minor	Usually not felt	900,000	0.0017
2.5 to 5.4	Light	Often felt	30,000	0.0039
5.5 to 6.0	Moderate	Slight damage to structures	500	0.092
6.1 to 6.9	Strong	A damage to populated area	100	0.18
7.0 to 7.9	Major	Serious damage	20	0.34
8.0 or greater	Great	Destroy all near epicenter	0.1 to 0.2	0.65

Table 2. Richter scale of earthquakes and its frequency of occurrence.

As shown in Figure 6, all seismic waves can be summarized into two types: body waves and surfaces waves. Body waves travel via the interior structure of the ground which can be divided in to two types: Primary waves and Secondary waves. Primary waves (P-waves) are propagated longitudinally in nature and Secondary waves (S-waves) are transversely. Surface waves travel along the surface of ground which are much slower and greater than body waves. However, damages caused by earthquakes are usually because of the great magnitude of surface waves. For modern seismology study and earthquake warning, high resolution seismometer which can detect the P and S waves are essential in the seismic motion system.

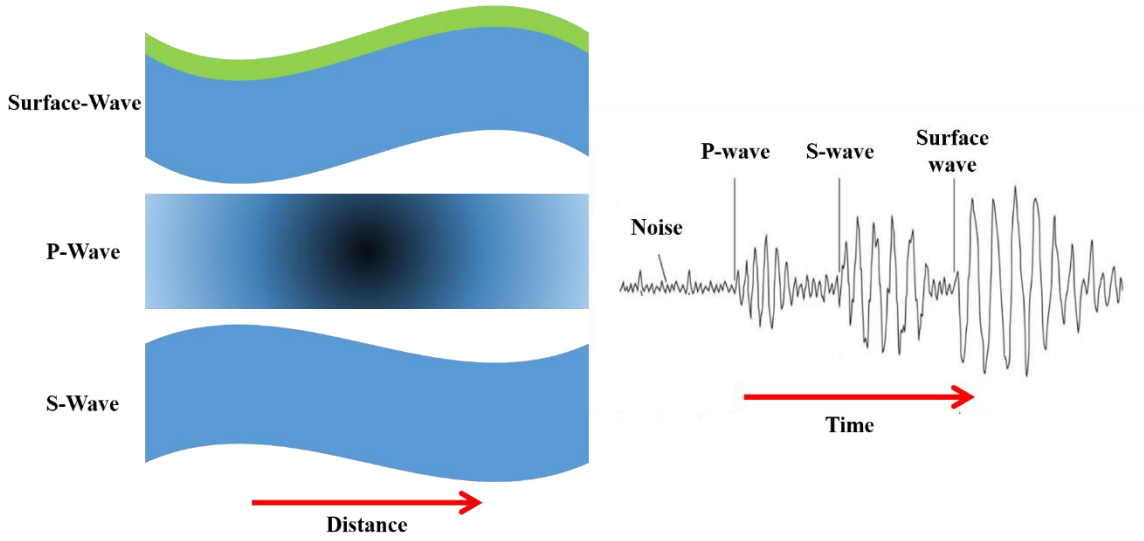

Figure 6. P-waves, S-waves and surface waves from seismograph

In order to sense both P, S and surface waves, the amplitude and frequency range of modern seismometer system is very large. Typically, 1nm displacement at 1Hz resolution is required for the purpose of research. The band of frequencies are from 10^{-5} to 10^{3} Hz. Table 3 indicates the frequency category of seismic sources. [10]

Frequency (Hz)	Seismic Sources
10^{-5} to 10^{-4}	Earth tides
10^{-4} to 10^{-3}	Earth resonant frequencies, earthquakes
10^{-3} to 10^{-2}	Surface waves, earthquakes
10^{-2} to 10^{-1}	Surface waves, P and S waves, Magnitude 6 earthquakes
0.1 to 10	P and S waves, Magnitude 2 earthquakes
10 to 10^{3}	P and S waves, Magnitude <2 earthquakes

Table 3. Typical frequencies generated by seismic sources.

Underwater Earthquakes

Comparing with ground earthquakes, underwater or submarine earthquakes are more difficult to be observed, due to the lack of accurate instrument for the application of marine exploration in harsh environment. As 71% of earth are covered by oceans, great earthquakes occur mostly beneath the sea floor. Although most high frequency seismic waves' energy are distorted during the propagation underwater, low frequency energy leads large damages such as the tsunami. In 2011 Japan, Tohoku earthquake, as the strongest known earthquake cause a series of disasters. 15,894 people were dead, 6,152 were injured and 2,562 people were missing in these disasters. What's worse, the tsunami caused nuclear accidents in Fukushima Daiichi Nuclear Power Plant. [11]

There was no related research of underwater earthquakes until 1937. A research group at Lehigh University of Pennsylvania, USA (Ewing and Vince) provided a system for the underwater seismology exploration. In 1949, Lamont Geological Observatory was established and other global institutions were joined and made efforts in developing Ocean Bottom Seismograph systems (OBSs). [12]

As shown in Figure 7, standard OBS system includes a broad-band seismometer, typically with 1~4.5 Hz resonant frequency, a high resolution data logger, batteries,

pressure vessels, long distance cables and GPS system. The total package of this heavy instrument can reach 600 kg in to the water.

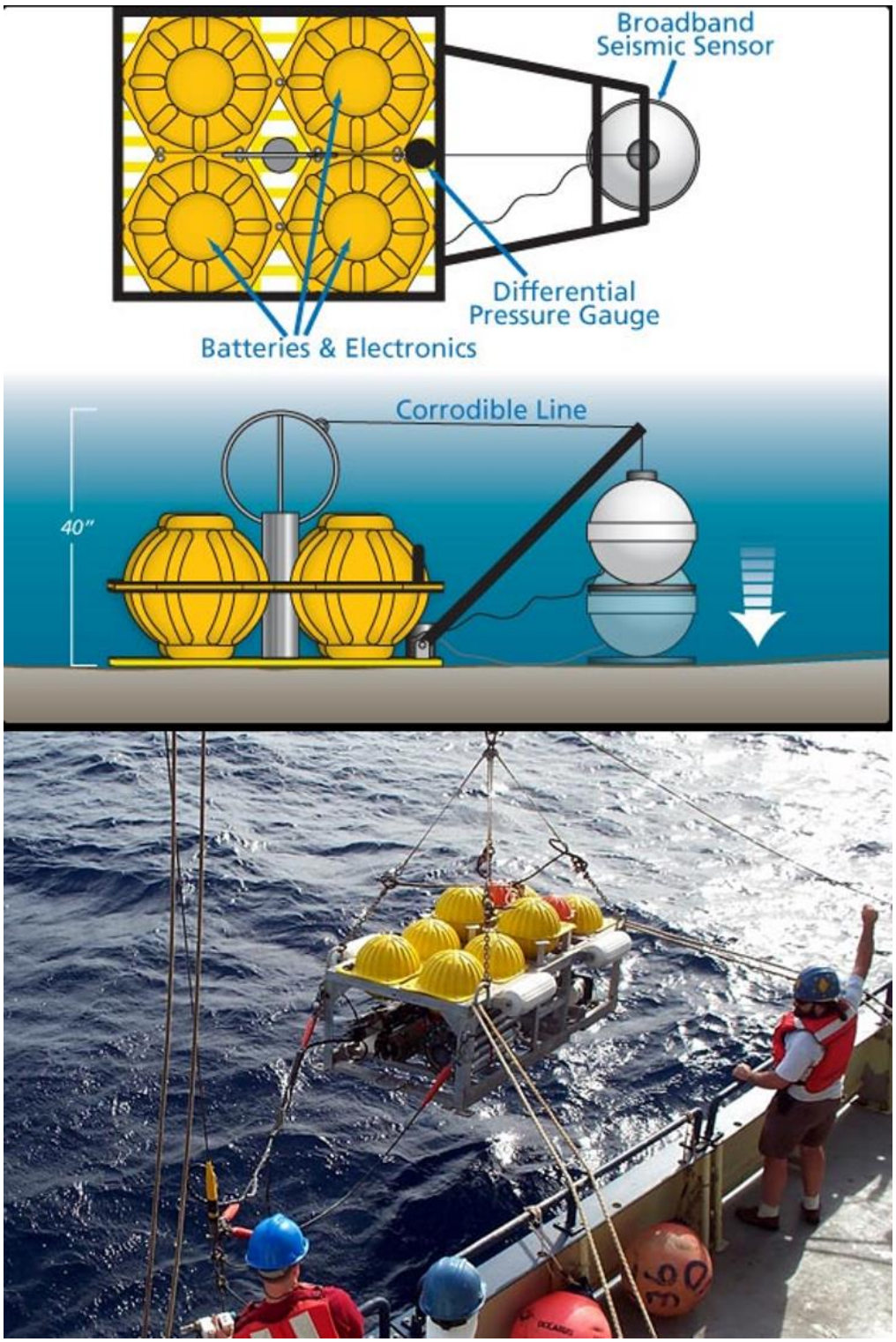

Figure 7. A long-term Ocean-Bottom Seismograph (Jack Cook, WHOI) (Photo by John Whitehead, Woods Hole Oceanographic Institution)

Planetary Seismic Exploration

The best way to know about the internal structure of a planet is to observe the seismic signals by using seismograph or seismometers. The seismic sensor networks on earth has been commonly used in precisely describing the interior structure of our earth. In 1969, Apollo 11 mission first time sent human onto the moon. One project in this mission was to install a modern seismometer on the surface of the moon to detect the moonquake shown in Figure 8. Besides Apollo 11, Apollo 12, 14, 15 and 16 successfully sent 4 other seismometers to make a connected seismic detect system on the moon. Those planetary seismometers were settled as a triangular form with approximately 1100 km on a side which was named as Apollo Passive Seismic Experiment (PSE) network. Each PSE included a vertical motion sensor with 0.05 Hz to 10 Hz frequency range and three orthogonal sensors with 0.004 to 3 Hz frequency range. Although, only 3 months' data were collected, those valuable data roughly indicated the structure of the moon. Similar to the earth, there are four kinds of moonquakes: impacts from other meteoroid, thermal movement, shallow moonquake and deep moonquake. However, the resonant frequency of moon was very different from the earth. These series of projects were commanded to turn off in July 30, 1977. [13, 14]

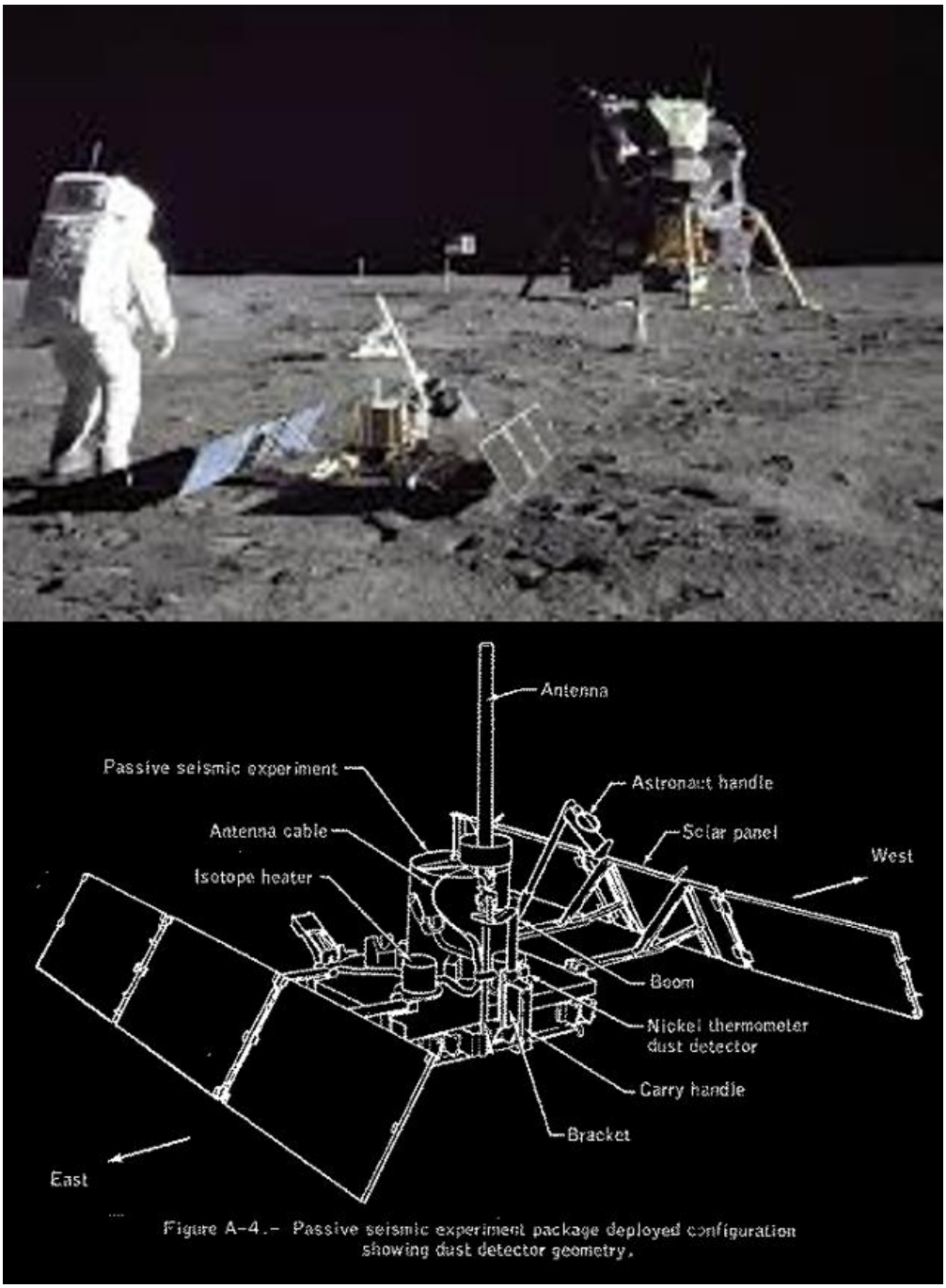

Figure 8 The Seismometer in Apollo 11 mission (lpi.usra.edu)

Besides the exploration of moon, National Aeronautics and Space Administration (NASA) is implementing its exploration agenda to the Mars and develop a sustained human presence there. As one essential part of mars mission, Insight mission, in terms of Interior

Exploration using Seismic Investigations, Geodesy and Heat Transport, tries to use robotic Mars lander to help install a series sensor on the surface of Mars including a high accuracy seismometer system. The core of the very broad band seismometer includes three one axis capacitive seismic sensors which are developed by Institut de Physique du Globe de Paris (IPGP) in France funded by the French national space agency. As shown in Figure 9 a suspended pendulum stabilized with a leaf shaped spring. The resolution is around 3 ng at 1 Hz with the resonant frequency below 10Hz. [15]

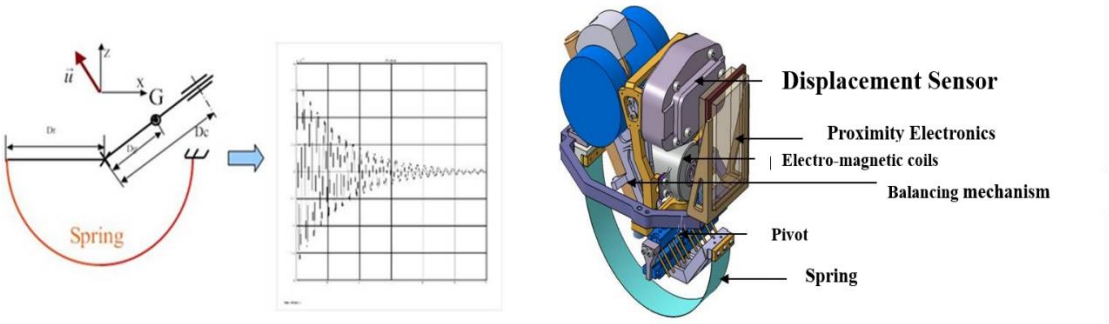

Figure 9 The Seismometer of Insight Mars Mission (insight.cnes.fr)

Recently in 2016, U.S. congress directed NASA to expand the mission of exploration the Europa by adding a small lander on its surface shown in Figure 10. As one of the largest moon of Jupiter, scientists have found the clues showing there may be salt-water ocean beneath a relatively thin and geologically active icy shell on its subsurface. It means Europa appears to meet the minimum requirements for life. In order to verify this guess, a seismometer is required in the mission to determine whether there is liquid water and how deep that water is. [16]

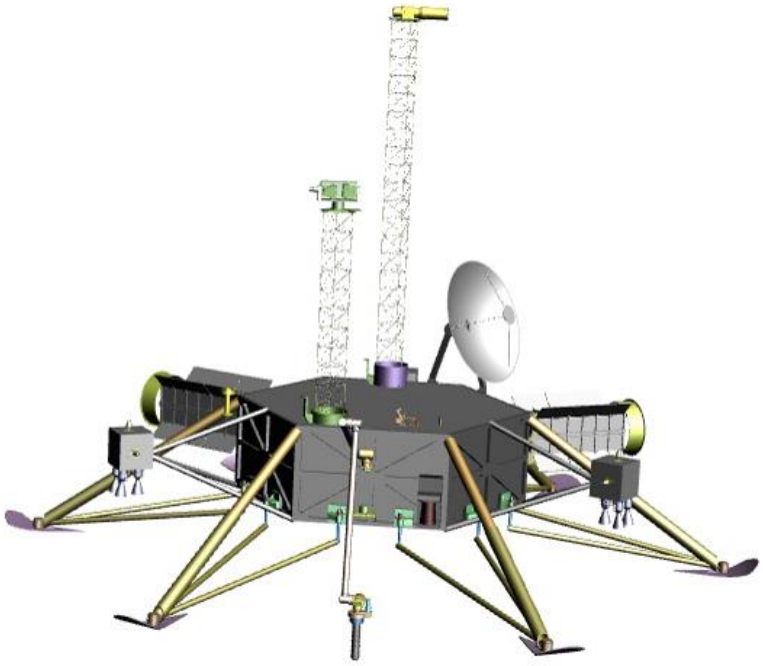

Figure 10 A Possible Lander with Tools for Europa (NASA)

State-of-The-Art Seismometers

The seismic instruments in early years consisted of large pendulum mass with springs. The data were recorded on soot-covered paper or photographic paper. Remarkable progress in seismological instrumentation has been developed in last few decades benefited from the progress of modern electronic technology and feedback control system. In engineering, the old seismographs converted the ground displacement into the mass displacement mechanically. [10] Modern technology in transducer provided mechanic-electro mechanisms to convert the ground motion into electrical signals related to the velocity or acceleration of the inertial mass. The most common mechanism is based electro-magnetic system, which includes a fixed coil within a magnetic field and a magnet as the inertial mass relative to the frame as shown in Figure 11 (a).

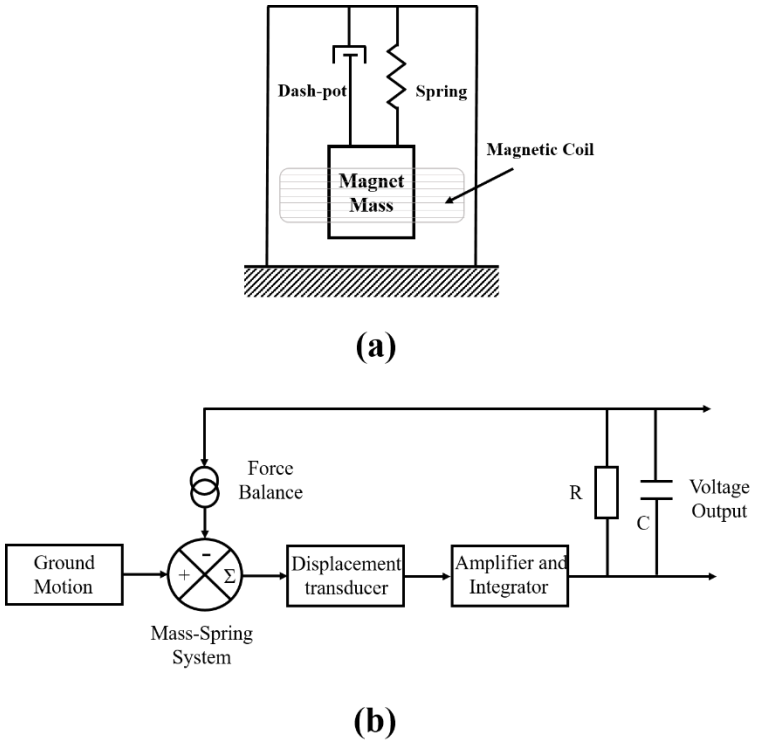

Figure 11 Electro-Magnetic Seismometer (1) Schematic (2) Feedback System

By introducing the electronic negative feedback loop into modern seismometers, the frequency bandwidth is significantly broad. As shown in Figure 11 (b), the electronic output of the seismometer excites the force balance transducer which can apply external force with desired phase shift to balance the resonant movement caused by the ground motion. This type of sensor is called Force Balance Accelerometer (FBA). The FBA technology is widely used in broadband velocity seismometer (VBB). Long period seismic detection can be achieved due to the improvement of VBB, in which the nature frequency of earth can be reached. Linearity is another factor can be improved by FBA system, which is 1000 times improved comparing with no-FBA system. Table 4 demonstrates some of the state-of-the-art VBBs, which are current widely used in the global seismic networks. [17]

Model	Self-noise ($m/s^2/Hz^{1/2}$)	Flat response	Proof mass
Streckeisen STS-2	3.16×10^{-11}	120 sec to 50Hz	14 kg
Gűralp CMG-3T	1.78×10^{-10}	120 sec to 50Hz	14 kg
Nanometrics Trillium 120P	5.62×10^{-10}	120 sec to 145Hz	11 kg
Nanometrics Trillium 240	1.12×10^{-10}	240 sec to 35Hz	14 kg
Geotech KS-1	9.25×10^{-11}	330 sec to 5Hz	43 kg

Table 4. Parameters of VBB seismometers

Capacitive micro-accelerometers or seismometers based on Micro-Electro-Mechanical System (MEMS) are another new trend of modern seismic instrumentation. The capacitive coupling is employed as the covert mechanism from ground motion to voltage output related to inertial mass's displacement. As shown in Figure 12, MEMS capacitive motion sensor provides a structure which can be fabricated by semiconductor-fabrication process and compatible with CMOS fabrication process.

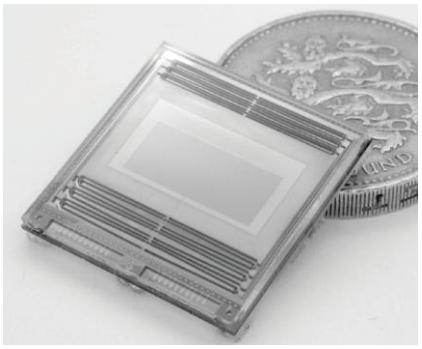

Figure 12 The packaged micro seismometer by Pike

MEMS accelerometers, gyroscopes have been widely applied in the consumer electronics as a part of navigation and sports-monitoring system. Differential capacitors are to sense the relative displacement of the inertial-mass to the reference substrate. Although, small proof-mass with rigid spring connection bring high resonant frequency comparing with traditional seismometer, MEMS accelerometer or seismometer has its advantages in low-self noise, high frequency range (advanced FBA) and low cost. The noise level of current MEMS motion sensor can only reach 5-20 $um/s^2/Hz^{1/2}$ at low frequency. The rapid improvement of MEMS-CMOS fabrication shows a promising future for these kind of low-power sensors. Table 5 indicates the current MEMS capacitive accelerometers. [18-25]

	Lemkin	Tseng	Qu	Sun
Sensing range (G)	± 1.4	± 6	± 3.2	± 6
Power dissipation (mW)	45	0.7	1	5
Sensitivity (mV/G)	N/A	191	520	0.53
Noise ($\mu G\ Hz^{-1/2}$)	110	354	12	120
	Wu	Chae	Freescale (MMA6361L)	ADI (ADXL203)
Sensing range (G)	± 6	± 1	± 6	± 1.7
Power dissipation (mW)	30	N/A	1.3	2.1
Sensitivity (mV/G)	130	490	206	1000
Noise ($\mu G\ Hz^{-1/2}$)	50	1.6	350	110

Table 5 Comparison of MEMS accelerometers

CHAPTER 2

INTRODUCTION OF MECHANISMS OF SEISMIC MOTION SENSING

Background of Molecular Electronic Transducer

Molecular electronic transducer (MET) belongs to a class of inertial sensors which are widely used as accelerometers, seismometers, tilt sensors and velocity meters. Unlike traditional solid-state mass-spring system, most liquid based motion sensors transduce the liquid movement caused by ground motion to electrical signal. As a kind of liquid motion sensor, a Molecular Electronic Transducer (MET) is sensitive to the flow of iodide electrolyte relative to fixed electrodes involving charge transport by solution of iodide ions. METs capture the physical and chemical reactions occur at the surface of charged electrodes in electrochemical cell as the result of hydrodynamic movement. The first development of electronic devices based on charge transfer via ions in solution was in the 1950s by US-Navy sponsored research which was named as "Solion". [26-28] It has been proved "Solion" based sensor have advantages in application of low-frequency acoustic wave detection such as infrasonic microphone and underwater pressure sensor. [29, 30] With the development of Russia's research group, MET was introduced in the inertial motion detection in terms of "Solion". [31] Inspired of "Solion" technology and micromechanical system (MEMS), high performance motion sensors such as, MET seismometer, accelerometer and angular sensor has been developed with small size and low cost. [32-34]

The seismometer for planetary exploration is an instrument that measures the seismic waves produced by quakes, impacts and other events on a planet. Due to its wide frequency spectrum and dynamic range of planetary seismic motion, a seismometer capable of recording vibration amplitude from 0.1nm to 10mm with a frequency between 0.01Hz to 100Hz is required for the seismic research. Design of planetary seismometers is fraught with difficulties. Broadband spring-mass system-based seismometers require the use of large proof masses to achieve low thermal self-noise; traditional seismometers with high performance are usually heavy, inconvenient for installation, highly dependent on installation angle, fragile and high cost. Compared with conventional seismometers based on a solid proof-mass-spring system, MET- based seismometers derive great advantages from using liquid as the sensing body on deployment, including high shock tolerance and no angle installation dependence.

Mass-Damped-Spring System in Inertial Motion Sensors

The measurements of inertial motion are done in a moving reference frame (the earth's or other planet's surface), so almost all inertial motion sensing systems are based on the inertia of a suspended proof mass, which will tend to keep static in response to external motion. The relative motion between the suspended proof mass and the ground will then be a function of the ground's motion. Figure 13 shows the simple schematic of inertial motion sensor which will detect the external motion horizontally.

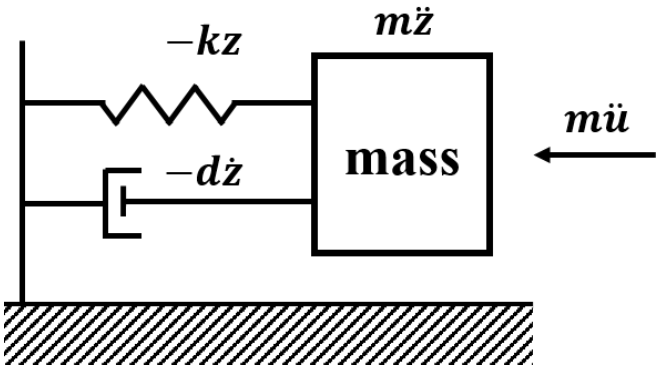

Figure 13. A schematic of an inertial motion sensor based on mass-spring damper.

The system contains a proof mass with the weight *m* suspended from a spring with spring constant of *k*, and a 'dash pot' with the friction constant *d* which applies the damping force to avoid the mass to swing excessively near the resonant frequency ω. Let $u(t)$ be the external horizontal motion and $z(t)$ the displacement of the liquid inertial mass *m* relative to the ground, both positive upwards. There are two real forces acting on the mass:

Spring force: $-kz$, negative because the spring opposes the mass displacement.

Damping force: $-d\dot{z}$, proportional to the mass times the velocity, negative since it also opposes the motion.

The acceleration of the mass relative to an inertial reference frame will be the sum of the acceleration with respect to the ground $\ddot{z}$ and the external acceleration $\ddot{u}$. According to Newtown's First Law, the sum of forces must be equal to the mass times the acceleration, we have:

$$-kz - d\dot{z} = m\ddot{z} + m\ddot{u} \tag{1}$$

By explaining the spring constant and friction constant with resonant frequency $\omega_0 = \sqrt{k/m}$ and damping constant $h = d/2m\omega_0$, the equation can be written as:

$$\ddot{z} + 2h\omega_0\dot{z} + \omega_0^2 z = -\ddot{u} \tag{2}$$

This equation shows that the ground acceleration can be obtained by measuring the relative displacement of the mass, z, and its time derivatives. Since an arbitrary signal can be described as a superposition of harmonics, the simplest way to solve Equation (4) is to assume an input of a harmonic ground motion and solve for the solution in frequency domain. Set the ground motion as

$$u(t) = U(\omega)e^{j\omega t} \tag{3}$$

where $U(\omega)$ is the complex amplitude and ω is the angular frequency. Since a seismometer can be assumed to represent a linear system, the mass relative motion is also a harmonic motion with the same frequency.

$$z(t) = Z(\omega)e^{j\omega t} \tag{4}$$

We then can have:

$$\ddot{u} = -\omega^2 U(\omega)e^{j\omega t} = a(\omega)e^{j\omega t} \tag{5}$$

$$\dot{z} = i\omega Z(\omega)e^{j\omega t} = V(\omega)e^{j\omega t} \tag{6}$$

$$\ddot{z} = -\omega^2 Z(\omega)e^{j\omega t} = A(\omega)e^{j\omega t} \tag{7}$$

Inserting Equation (7)-(9) to Equation (4), and dividing by the common factor $e^{j\omega t}$, we can obtain the relationship between the output and the input signal in frequency domain. Almost all traditional seismometers are inductive type seismometers which have fixed coil and a magnet moving with the mass. The output voltage from the coil is proportional to the velocity of the mass relative to the frame. However, MET inertial sensor directly converts the acceleration of the proof mass to current signal by detecting the change of electrochemical reaction. The transfer function between output current to external acceleration can be described as:

$$H_a(\omega) = \frac{A(\omega)}{a(\omega)} G = \frac{-G}{\omega_0^2 - \omega^2 + i2\omega\omega_0 h} \tag{8}$$

where G is the generator constant which relates the acceleration of the mass (relative to the frame) to the output current, in the unit of A/(m/s^2).

One of the most important factor of inertial motion sensor is the resolution which reflects the smallest detectable acceleration signals. The instrument noise comes from both the electronic noise and the mechanical noise of the mass-spring system. The electronic noise is generally well quantified for the amplifiers and the feedback circuit. The fundamental limit to the mechanical self-noise is set by the Brownian motion of gas molecules hitting the proof mass. Usher [35] shows the noise-equivalent acceleration (NEA) for a unit bandwidth at any frequency is given by

$$NEA^2 = 4k_B T \frac{\omega_0}{mQ} \tag{9}$$

where k_B is the Bolzmann constant, T is the temperature in Kelvin, $Q = \omega_0 m/d$ is the quality factor which measures the energy stored versus the energy loss per cycle for a mass-spring system. NEA is expressed in the unit of $m/s^2/\sqrt{Hz}$. Therefore, motion

sensors with high Q , large mass and long period (low working frequency) have lower self-noise and higher resolution.

Room Temperature Ionic Liquid based Iodide Electrolyte

It is known that classical solutions of electrolytes are consisted of dissolution of salts in molecular solvent, such as water based electrolyte. Such system includes solvated ions, their charged or neutral combinations and solvent molecules. Otherwise, a salt can be liquefied by providing heat to the system to counterbalance the salt lattice energy. We called such system molten salts or Ionic Liquid (IL). ILs only consist of ions and their combinations without any molecular solvent. Those ILs, salts molten at room temperature or below, form a new class of liquids named Room-Temperature Ionic Liquid (RTIL) with very interesting properties, such as high chemical, thermal and electrochemical stability, high conductivity, no measurable vapor pressure and non-flammability. [36, 37]

The first IL was disputed in 1888 by S. Gabriel and J. Weiner, which was Ethanolammonium nitrate with melting point around 55°C. [38] In the middle of last centuries (1948), the first RTIL was patented which was based on chloroaluminate anion. [39] Since then, with decades of development, ILs as a kind of green chemistry, are widely used in pharmaceuticals, cellulose processing, gas handling, nuclear fuel reprocessing, solar cell development, waste recycling and safety improvement in lithium batteries.

One of the interesting property of ILs is their tenability, as each IL consists of an anion and a cation which can be mixed and matched to obtain the desirable properties. By mixing ILs with other liquids such as water, more useful properties can be tuned. [40] Those mixtures have been found important in use of electrical applications such as electrolytes for dye-sensitized solar cell and the electroplating of zinc films. Most previous MET motion sensors used water based iodide solution which has been widely used in the earth ground motion detection. However, applications in harsh environments, such as planets

exploration in space, oil detection and deep-sea research requires wider operation temperature range, high resolution, high sensitivity and long surviving time which are not feasible for water based electrolyte. Accordingly, ionic liquid as a kind of "green solvent" which usually has higher iodine ion solubility and is often fluid in wider temperature range than water, has been proved to improve the performance of MET accelerometer including sensitivity and working temperature range. AS most traditional MET sensors used water based iodide solution as the sensing body, the performance is highly dependent on the concentration of iodide ions, which is sensitive to the temperature change. Moreover, water based solution is limited by its vapor pressure in application of high or low pressure circumstance. Consequently, Ionic Liquids (ILs), salts molten at room temperature, have remarkable properties widely in use of electrochemical devices, such as high thermal, chemical and electrical stability, high conductivity, no measurable vapor pressure and high solubility of iodide ions.

Introduction of Galvanic Cell

Luigi Galvani, an Italian physician, firstly discovered that when two different metals such as copper and zinc are connected and touched the different parts of a nerve on frog's leg at the same time, the leg will contracts. He named the phenomenon "animal electricity". This discovery paved the way for modern electrical batteries. As the results, people named those an electrochemical cells that derive electrical energy from spontaneous redox reactions taking place within the cell as "Galvanic Cell".

A typical cell consists of two types of metal, zinc and copper, each immerses each in a solution containing a dissolved salt of the corresponding metal shown in the Figure 14.

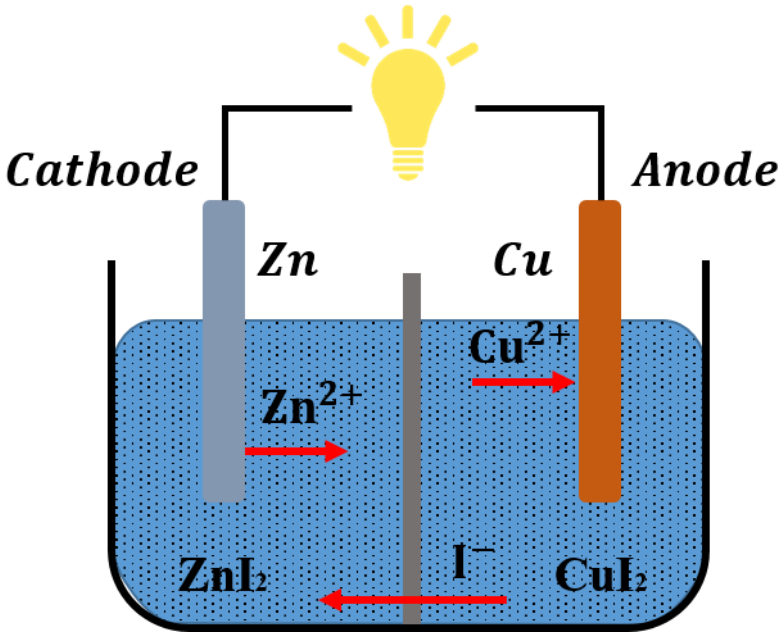

Figure 14. Schematic of Galvanic cell without flow

The two solutions are separated by a porous barrier that prevents them from rapidly mixing but allows ions to diffuse through. In electrochemistry, we called it salt bridge. When the copper and zinc plates are connected by conductive connections, the excess electrons flows from Zinc to Copper through external connection as Zn^{2+} are emerged from

Zn and Cu^{2+} ions will convert to Cu atoms at the surface of copper plate. In this electrochemical reaction, zinc plate is treated as Cathode and copper as Anode. The reaction is the oxidation of Zn by Cu^{2+} ions:

$$Zn(s) + Cu^{2+} \rightarrow Zn^{2+} + Cu$$

$$Zn(s) \rightarrow Zn^{2+} + 2e^{-} \qquad \text{Oxidation at Cathode}$$

$$Cu^{2+} + 2e^{-} \rightarrow Cu \qquad \text{Reduction at Anode}$$

Besides electrochemical batteries, Galvanic Cells are widely used in moisture sensor and oxygen sensor, in which the humidity of air and oxygen content will affect the electrical potential between anode and cathode.

CHAPTER 3

MOLECULAR ELECTRONIC TRANSDUCER BASED

MOTION SENSOR

Operation Principle of Molecular Electronic Transducer Mass-Spring System

As shown in Figure 15, a MET sensor, for example, MET seismometer, includes a sensing element consisting of four layers of platinum electrodes and five layers of insulation [33]. The sensing element contains four electrodes configured as Anode-Cathode-Cathode-Anode (ACCA) parallelly separated by die-electrical spacers. The sensing element, together with the electrolyte as the sensing body, is sealed in a ceramic tube by a silicone rubber membrane at both ends. Each anode-cathode pair is an electrochemical cell, in which charges are transferred between anode and cathode by ions in the electrolyte. Traditionally, standard machined platinum (Pt) mesh is used to make the electrodes, and plastic or ceramic grids produce the dielectric inter-electrode spacers [30]

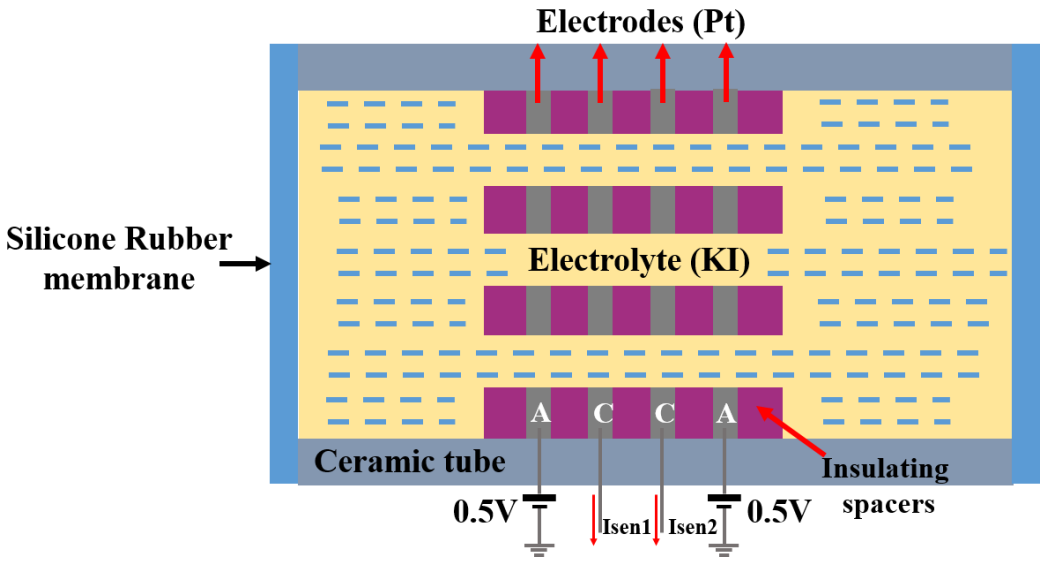

Figure 15: The MET seismometer schematic view without external vibration

An alternative approach to build the sensing element is to combine MET and MEMS techniques which improve the alignment between each channel and reduce the internal dimensions of electrodes below 1μm which improved the resolution and reproducibility of the whole system. [41]

The sensing mechanism of the MET motion sensor is based on the charge transfer caused by reversible electro-chemical reaction between anode-cathode pairs via electrolyte ions in iodide solution. Typically, the electrolyte used in a MET sensor is a water-based solution containing potassium iodide (KI) with a small amount of iodine (I_2). Four electrodes are in contact with the iodide electrolyte; when applying 0.5V voltage, the difference between electrodes will generate current signals in the device. The electrodes are assigned as Anode-Cathode-Cathode-Anode (ACCA); applying opposite-direction voltage to left and right pair of electrodes results in a reversible chemical reaction in each pairs as follows:

On anodes, generation of tri-iodide:

$$I_2 + I^- \rightarrow I_3^- \tag{10}$$

On cathodes, reduction of tri-iodide:

$$I_3^- + 2e^- \rightarrow 3I^- \tag{11}$$

When there is no applied acceleration, the static electrochemical reaction generates background current at the cathodes, which can be explained as [32, 33, 41]:

$$I = Dq(\oint_S (\nabla c, \mathbf{n}) dS) \tag{12}$$

where D is the diffusion coefficient, ∇c is the concentration gradient of the active charge carriers within the AC pair, q is the charge transferred across the interface in single

electrochemical reaction, ***n*** is a unit vector normal to the surface of the electrode, and the integration is done over *S*, electrode surface area. Here only diffusion is considered as mechanism responsible for the active ions transport in the electrolyte volume. The migration is not included due to the screening of the electrical field in the highly concentrated electrolyte and the convection does not contribute to charge transfer through the electrode surface due to zero-velocity condition on the solid surface.

In the presence of external acceleration applied on the ceramic tube pointing to the left as shown in the Figure 16, inertial force will cause an electrolyte flow to the right. There are two forces acting on the electrolyte because of the movement: restoring force from silicone rubber relative to the displacement of electrolyte mass and hydrodynamic damping force from hydraulic impedance proportional to the electrolyte flow speed through the micro-sized channels. The whole structure can be described as a fluidic spring mass system.

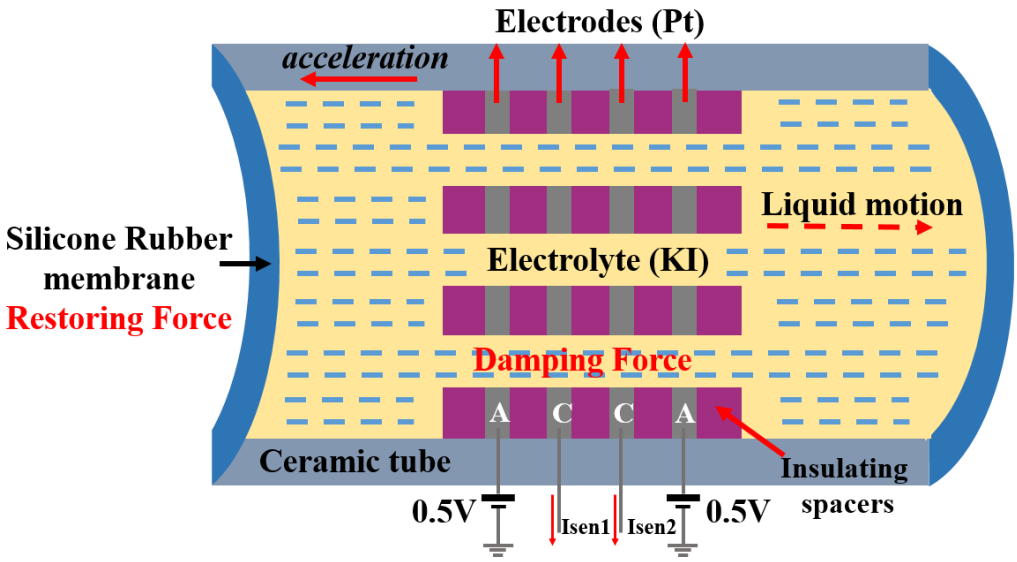

Figure 16: The MET seismometer schematic view with external vibration

When there is no or only static mechanical motion applied to the system, the electrochemical (background current) is only associated with the diffusion of ions, in which the tri-iodide ion concentration shows a symmetric gradient between two AC pairs shown in Figure 17(a). As the geometry of four electrodes is symmetric, the background currents of two pairs AC electrodes are equivalent. By applying dynamic mechanical motion input to the system, electrolyte in the channel flows to the opposite direction because of inertia. It causes a change of concentration of active ions as shown in Figure 17(b).

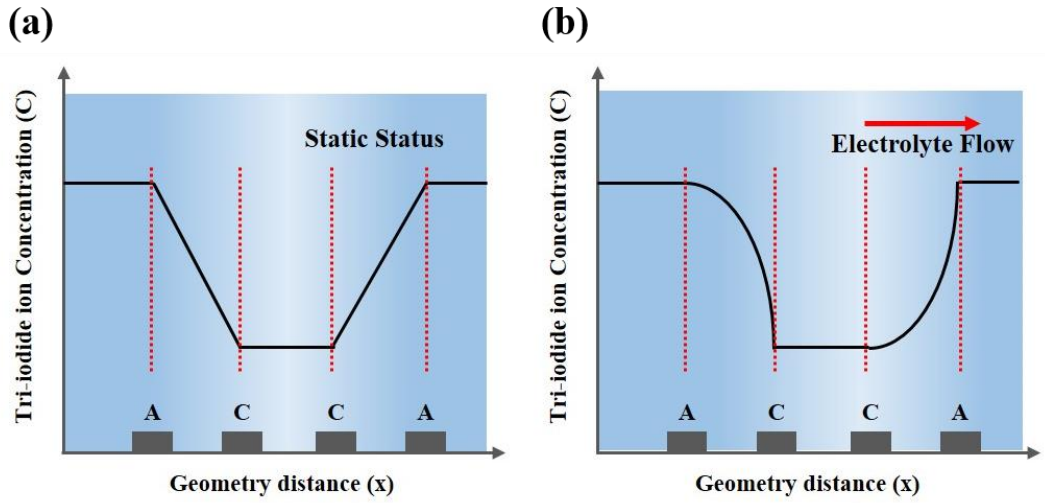

Figure 17 Tri-iodide concentration gradient for MET sensor

An unsymmetrical concentration gradient pattern occurs around two AC pairs. When mathematically making a differential to the two currents, background currents will be cancelled and differential signal will be amplified, which is given by:

$$I_{out} = I_{C2} - I_{C1} = Dq\left(\oint_{S_{C2}} (\nabla c_1, \mathbf{n}) dS_{C2} - \oint_{S_{C1}} (\nabla c_2, \mathbf{n}) dS_{C1}\right) \quad (13)$$

where I_{C1}, I_{C2} are the currents through the surface of the corresponding cathodes, S_{C1}, S_{C2} are the surface areas of the corresponding cathodes.

Transfer Function of Dynamic Response

In order to study the signal conversion of MET motion sensor in dynamic vibration condition. It be described in two processes: the conversion from vibration to liquid flow by mechanical system; the conversion from flow of electrolyte to current signal by electrochemical reaction:

$$H(\omega) \approx H_{mech}(\omega) \cdot H_{ec}(\omega) \tag{14}$$

where H_{mesh}: mechanical response of the fluidic system, H_{ec}: the ability of the electrochemical system to detect electrolyte motion as a function of frequency.

To study the mechanical response of MET system, a simple derivation of standard oscillating system transfer function helps in which PDMS diaphragm applies restoring force and damping force comes from the hydrodynamic resistance of the channel. The equation that governs motion of the electrolyte can be expressed as:

$$\frac{dQ}{dt} + \frac{R_h S_{ch}}{\rho L} Q + \frac{k}{\rho L} \int_0^t Q \, dt = -S_{ch} a \tag{15}$$

where Q is the volumetric flow of fluid passing through the channel,, a is the external acceleration, R_h is the hydrodynamic resistance which is solely determined by the channel geometry in laminar flow condition, k is the coefficient of volume stiffness and depends only on the characteristics of the membrane, ρ is the density of the electrolyte, S_{ch} is the cross-section area of the channel and L represents the length of the channel, filled with electrolyte. By transforming the time domain equation in to frequency domain, the transfer function of mechanical motion in fluid can be expressed as:

$$|H_{mech}(\omega)| = \left|\frac{Q(\omega)}{a(\omega)}\right| = \frac{\rho L}{\sqrt{(\frac{\rho L}{S_{ch}})^2 \frac{(\omega^2-\omega_0^2)^2}{\omega^2} + R_h^2}}, R_h = \frac{8\mu L}{\pi r^4} \quad (16)$$

where μ is the viscosity of electrolyte, r is the inner channel radius and and L represents the length of the channel.

According to the description from Larcam's study of "Solion" device in 1964 [16], a simple derived model can represent the electrochemical system as:

$$|H_{ec}(\omega)| = \left|\frac{I(\omega)}{Q(\omega)}\right| = \frac{C}{\sqrt{1+(\frac{\omega}{\omega_D})^2}} \quad (17)$$

where C ($A/(m^3/s)$) is the conversion factor of the electrochemical cell which depends on the geometry of ACCA electrodes, $\omega_D = D/d^2$ is the diffusion frequency and d is the distance between AC pairs.

Noise

To MET sensors, the thermodaynamic self-noise, convention-included self-noise, and geometry noise contribute to the self-noise dominantly. [42]

- Thermodyanamic Self-Noise

The thermodynamic Self-Noise is employed by the disturbance of liquid caused by the pressure difference on both sides of MET channel. In units of input acceleration, this noise spectral density is independent from frequency:

$$\langle a \rangle^2{}_{\omega} = \frac{2k_B \cdot T \cdot R_h}{\rho^2 L^2} \tag{18}$$

where T is the absolute temperature, k_B is Boltzmann's constant.

- Convection-Induced Self-Noise

The convection-induced self-noise comes from the natural convection of the liquid. [43] Even under a stable situation, small local vibrations of liquids will cause flows in the channel. Those flows generate current noise at output of MET sensors. Although those noises are difficult to be analyzed, people found the value of the convection induced self-noise depends on the Rayleigh number (Ra) of the electrolyte. It has been proven both experimentally and numerically that the convection self-noise decreases as Ra decreases.

- Convection-Induced Self-Noise

The geometry self-noise is proportional to the electrochemical part of the transfer function of MET transducer. To calculate the geometry self-noise, the following equation can be used:

$$\langle v \rangle^2{}_f = \beta \frac{4k_B T}{R_h} \overline{k_f}^2 \alpha^2 \tag{19}$$

where $\overline{k_f}$ is the averaged electrochemical part of the transfer function, α is the transducer conversion coefficient from output noise current to input noise velocities, and β is an empirical coefficient. The geometry noise is the dominant one at very low frequency.

Design of Peripheral Circuits and Vibratory Test Setup

In electronic circuits design, trans-impedance amplifier is an amplifier which converts current to voltage. Generally idea is to use a high value resistance connected with ground to convert the current signal to voltage one. However, the output impedance of the devices may vary at a very high range which will influence the potential on the resistance. As a result, an op-loop amplifier is applied to isolate the input current signal and the voltage output signal is based on the high input impedance of CMOS amplifier.

Instrumentation amplifier is a type of differential amplifier outfitted with input buffer, which has a very low DC offset. With low input referred noise and high open-loop gain, instrumentation amplifier has a satisfactory performance when using at MEMS sensors with low power supply. With 3 composed op-amps, it can both fulfill the high input impedance and controllable high gain with adjust the R_{gain} which is shown in Figure 18.

As the output current signals from two AC pairs contain two parts: equivalent background currents and unsymmetrical currents associated with external vibration. The recording circuits helps to cancel the background signal and amplify the differential signal as shown in Figure 18(a), which starts with a trans-impedance amplifier with 1000 Ohms gain. Then two amplified voltage signals are differential amplified by AD620 industrial amplifier with gain of 100 V/V. Considering that the noise from circuits has bad effect to the resolution of the whole system. AD822, FET-input amplifier with low input current noise of 18fA is chosen which is far below the noise floor of MET accelerometer sensing element at low frequency. As illustrated in Figure 18(b), the test setup includes a low frequency electromagnetic powered shaker, a seismic 10V/g low frequency reference

accelerometer from PIEZOTRONICS[INC] with the model of 393B31, Nation Instrument 6000 series data acquisition.

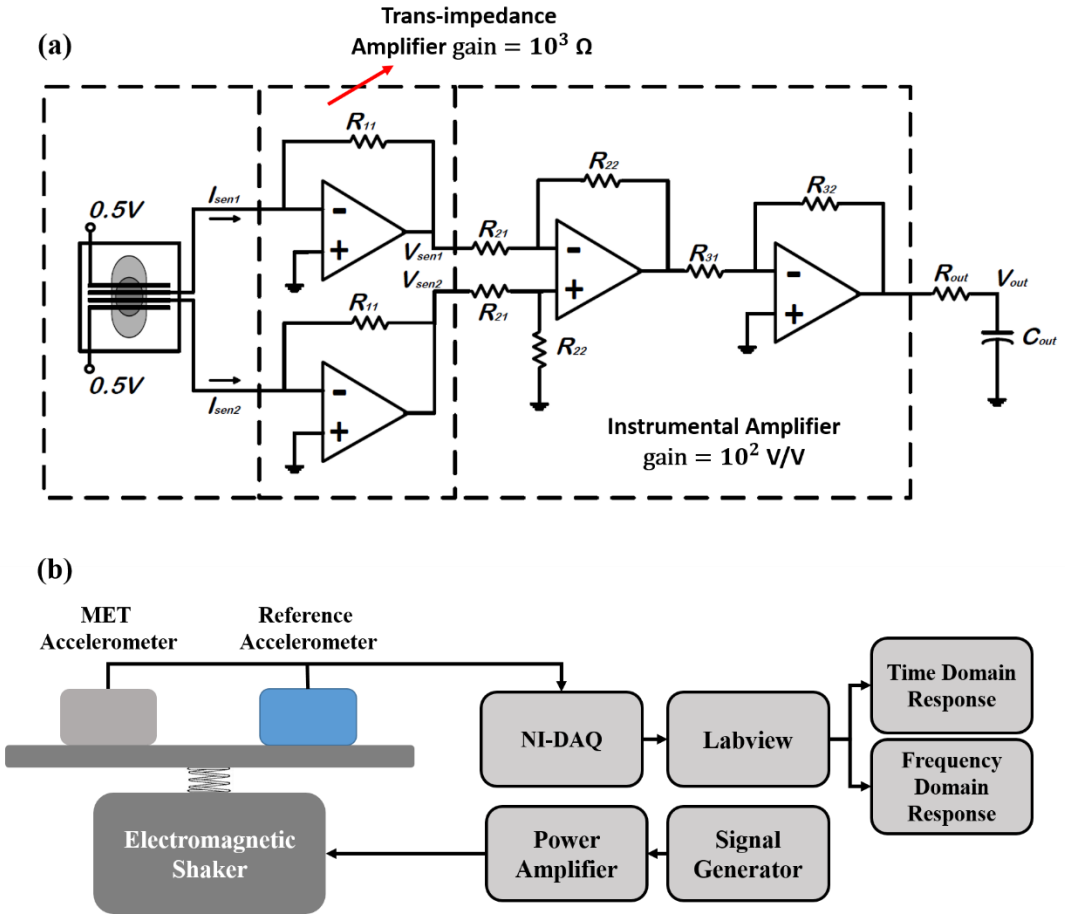

Figure 18 schematic of circuit design and test setup for MET motion sensor (a) peripheral circuit of MET sensor includes trans-impedance amplifier, instrumental differential amplifier and band-pass filter. (b) test setup of MET sensor includes a reference accelerometer, data record system and mechanic shaker control system

CHAPTER 4

DEVELOPMENT OF MET PLANETARY SEISMOMETER

Design and Micro-Fabrication on SOI Substrates

The core component in the MET seismometer is the molecular electronic sensing element. A commercialized MET seismometer uses platinum gauze as electrodes and a plastic grid as dialectical spacers. Due to the lack of control resolution in the alignment process, those devices suffer from low reproducibility and a limitation on performance optimization. Our previous work by Hai Huang shown in Figure 19 combined MEMS and MET technology and developed a structure containing four e-beam physical vapor deposited (E-beam PVD) platinum layers with a plasma-enhanced chemical vapor deposited (PECVD) silicon nitride (Si_3N_4) as an insulation layer and through holes milled by a focus ion beam (FIB) system (Nova 200 NanoLab, FEI). The combining of MEMS and MET technology has advantages in small size, high shock tolerance, high sensitivity and low noise, especially at low frequency. With the FIB etching process, we have successfully increased the number of channels on a single MET device from one to fifty. The simulation and experiment results of previous work indicated that the more channels formed on a single MET device, the lower the hydrodynamic resistance resulting from lower thermal dynamic self-noise. [32, 33] However, low throughput, high cost and the re-deposition issue of the FIB process limit the number of channels in one single MET device. Nevertheless, it is difficult to etch multiple platinum layers by another process. Instead of trying to resolve the etching dilemma, in this paper we have developed a novel fabrication process.

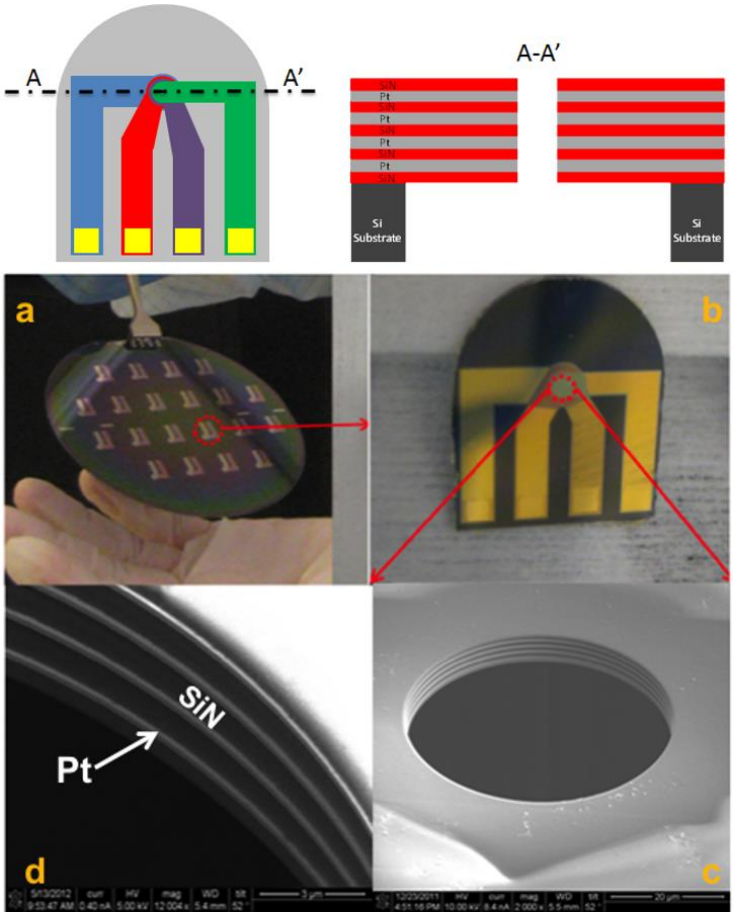

Figure 19. A schematic drawing and photos of Hai's micro seismometer sensing element (single channel) (a) 20 batch fabricated devices on one wafer. (b) A single-50 μm diameter-channel micro MET seismometer core. (c) SEM image of the through hole milled by FIB on the 5.8 μm thin diaphragm. (d) SEM image of the side wall of the through hole, showing exposed alternating Pt and SiN layers.

Critically, the number of micro-channels in MET four-electrodes sensing element, the quality of alignment of each layer and the length of each channel determine the hydrodynamic impedance. Our previous work developed a structure on top silicon wafer by depositing four thin layers of E-beam physical vapor deposited (PVD) platinum separated by plasma enhanced chemical vapor deposited (PECVD) Si_3N_4 insulation layers

and milling through each layer with focus ion beam (FIB) system (Nova 200 Nanolab, FEI). Although, the MEMS microfabrication technology successfully optimized the alignment quality and channel layout, low throughput, high cost and the re-deposition issue of FIB process limited the number of channels in single MET sensing element. Instead of trying to resolve the platinum etching process, in this paper, we demonstrate two alternative MEMS based designs on silicon on insulator (SOI) wafers.

Single-SOI Fabrication Process

As illustrated in Figure 20, the new fabrication process starts with SOI wafers, with the top device layer of 150µm, a box silicon dioxide layer of 5µm and a bottom silicon bulk substrate of 500µm. The first step is to pattern a circle shape etch mask with 10µm thickness AZ4620 positive photoresist on the bottom of the SOI wafer. Then the bulk layer is thinned down to 150µm to form the cavities by a deep reactive ion etching (DRIE) process. After cleaning the photoresist mask with 200 watt oxygen plasma, we span and pattern 5µm thickness AZ4330 positive photoresist for an etch mask with an array of 200µm diameter holes on the top of the device layer. Then, the device layer is etched by DRIE and stops at the SiO2 box layer to create channels 200µm in diameter and 150µm in depth. Without removing the photoresist, the SiO2 box layer is etched through with a buffered oxide etching (BOE) solution to expose the bulk layer; recesses are formed due to the undercut. The remaining 150µm bulk substrate layer is also etched by DRIE to open all of the channels. The AZ4330 photoresist is then removed by acetone and oxygen plasma. Then, a thin layer of Ti/Pt is E-beam deposited on both sides of wafer, and sidewalls of the channel holes are covered as well due to the rotation of sample holder. Finally, two

fabricated wafers are bonded with the above process through an intermediate Parylene-C layer to form a sensing element with four isolated Pt electrodes.

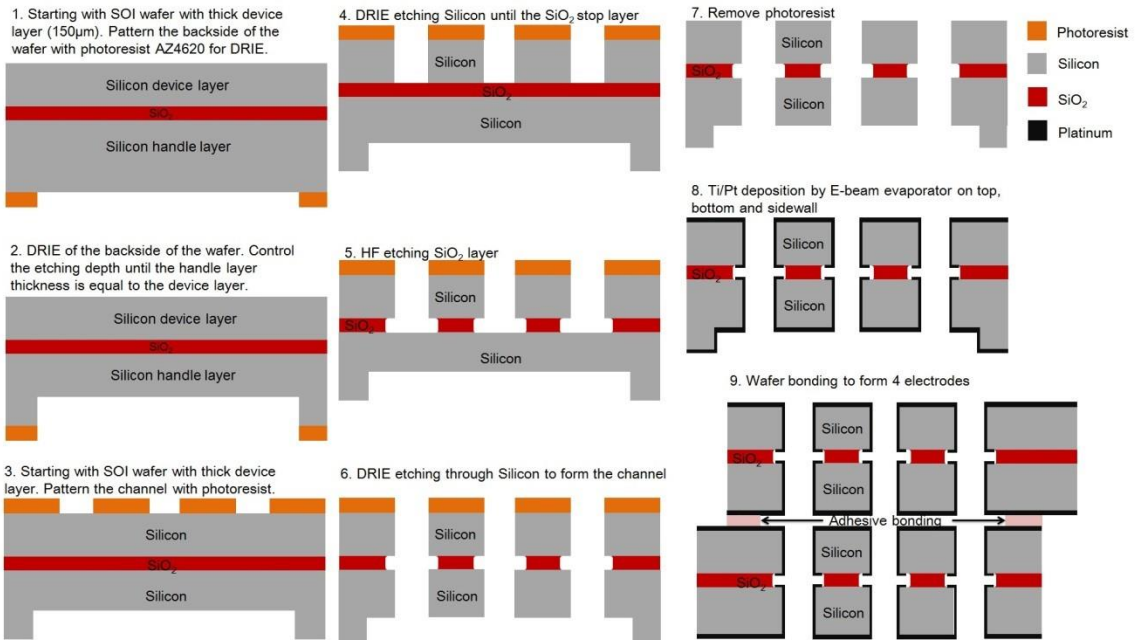

Figure 20. Fabrication processes of current MET based Single-SOI sensing element by Hai & Mengbing

This process produced sensing elements with 800 channels without the Pt etching process. Figure 21 shows the optical photos of test assembly, diced chip and the SEM image for the sidewall of holes. Diced chip is placed between two ceramic housings, including a pass-through channel. Ends of the channel are covered with a flexible, chemically inert rubber membrane. Two metal frames press all assembly parts together with a soft O-ring. The electrolyte is then filled under vacuum. As we chose a slow etching recipe for DRIE, the roughness of channel sidewalls is less than 200nm. The SEM photo illustrates that the platinum fully covers the sidewalls and the undercut of the two SiO2 insulated electrodes.

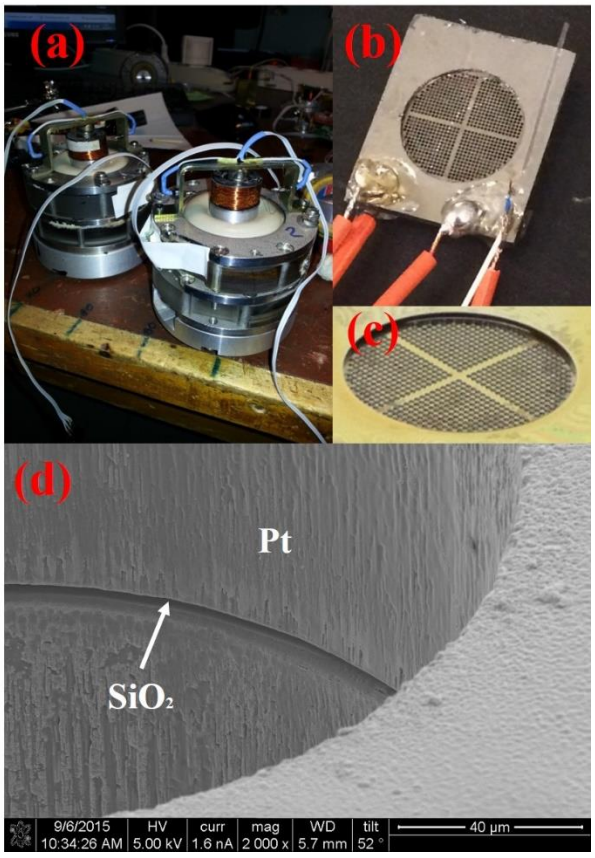

Figure 21 Photographs (optical and SEM) of a fabricated MET seismometer sensing element showing (a) test assembly; (b) the sensing element with its wire connection by conductive epoxy; (c)a schematic of the 800 channel structure and (d) an SEM photo of the Ti/Pt covered sidewall of each channel and the SiO2 under cut.

Double-SOI Fabrication Process

Although the above single-SOI based design overcomes the cost and throughput limitation of FIB based design, the channel length is increased from 5µm to 600µm which brings a notably increase of hydrodynamic impedance in each channel. However, it is extremely challenging to thin down the SOI bulk substrate by control the etching time and rate. To further reduce the channel length, we employed an alternative process based on double-SOI wafer.

As shown in Fig. 4, the design starts with a double layer SOI wafer with 5 layers: top device (DT), top box (BT), middle device (DM), middle box (BM) and bulk layer, in which DT=DM=5µm, BT=BM=2µm and <100> bulk layer=500µm. The first step is to use low pressure chemical vapor deposition (LPCVD) Si_3N_4 to cover both sides of D-SOI wafers. Secondly, the backside substrate is patterned with cross shape opening by AZ4330 photoresist and etched by reactive ion etching (RIE) with CF_4 gas. After removing the photoresist, the patterned LPCVD Si_3N_4 is applied as the hard mask for tetramethylammonium hydroxide (TMAH) anisotropic wet etching until it stops at the BM layer. As the substrate is <100> silicon substrate, the etched opening is a squared trench with a 54.7° slope in improved roughness comparing with DRIE etched side wall. Then, the backside Si_3N_4 mask is removed by RIE. Afterwards, a 1µm AZ3312 photoresist is spun on the topside and pattern with 200µm circle. The topside Si_3N_4 layer is then etched by RIE and DRIE with slower recipe is applied to etched through the DT layer to the BT layer. The roughness on the sidewall is limited in 200nm. After that, BOE isotropic etching of BT is performed to form the undercut which is desired to isolate two electrodes, while the BM is protected by photoresist and Teflon tape. To the next, DRIE will continue to etch the exposed DM layer until the whole channel opening is etched through. Similar to the single-SOI processes, rotated E-beam evaporation of thin metal of Ti/Pt is provided to form electrodes on top, bottom, sidewall of the channel, except the undercut area. Finally, Parylene-C adhesive layer is selectively deposited and two above fabricated wafers are adhesively bonded with alignment to complete the device.

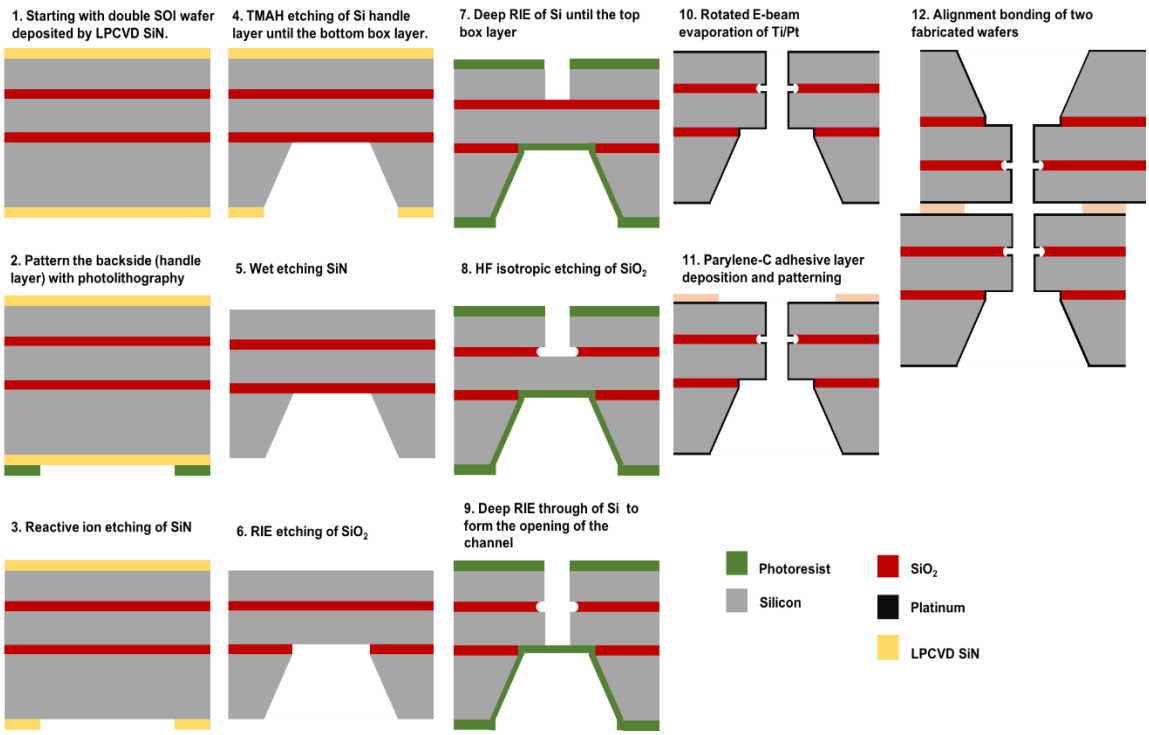

Figure 22. D-SOI based micro-fabrication process flow

The SEM photos shown in Fig. 23 indicates the layout and quality of a single channel in MET sensing element which fabricated by Double-SOI process.

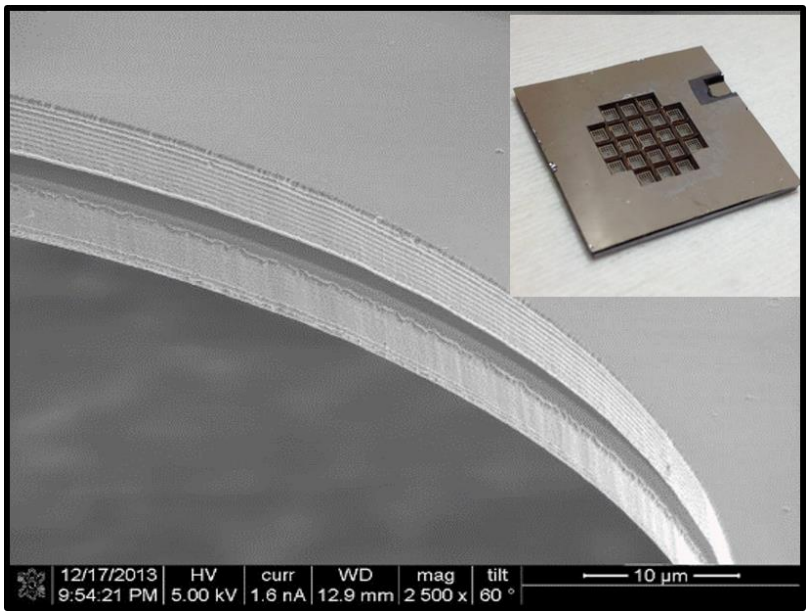

Figure 23. SEM photo of D-SOI based MET Sensing Element

Experimental Results and Discussion

The MET seismometer sensing element is assembled and tested at the Center of Molecular Electronics Research in Moscow, Russia. The packed device associated with its control circuit and magnetic feedback system is installed on a low frequency motion exciter controlled by a signal generator. Harmonic scan is used for dynamic response detection. The whole system is sequentially tested under 0.08Hz to 80Hz vibration with an approximately constant amplitude of 8.4μm/s in unit of velocity. Figure 24 shows the open-loop sensitivity spectrum in terms of the ratio between output current and motion exciter's current power in unit of seismic data-log digital counts, which indicates this device can reach 2500V/(m/s^2) sensitivity at 1 Hz with 0.3V voltage bias at the anodes. The results indicate that the first resonant frequency of the whole system is around 2Hz and second resonant frequency is around 150Hz. These two values reflect the ω_0 and ω_D in equations (24) and (25), where ω_D is usually the second one [44]. Accordingly, the sensitivity at first resonant frequency ω_0 benefits from the reduction of hydrodynamic resistance in terms of number of channels.

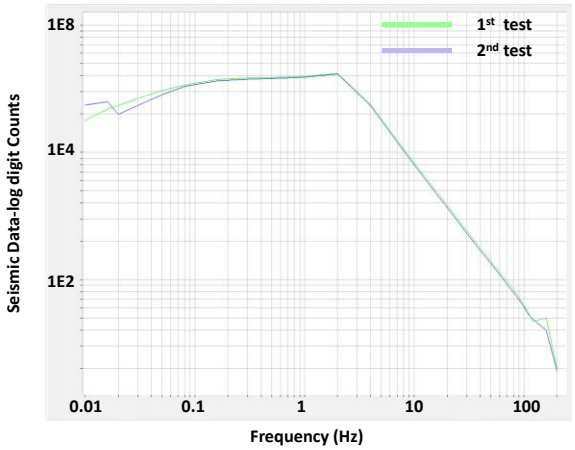

Figure 24. Sensitivity response of the 800-channel MET seismometer.

The viscosity of iodide electrolyte μ is 10^{-3} N/(m^2/s) and density ρ is 1.168 g/mL. According to Equation (16) and (18), we can estimate the noise and hydrodynamic impedance of three different designs as shown in Table 6.

	Channel number	*Length of sensing core (l)*	*Radius (r)*	R_h *(N/(m^5/s))*	Noise (m/(s^2×√Hz) in dB)
FIB	50	5.8 μm	50 μm	7.56×10^8	-133.38
Single-SOI	800	644 μm	200 μm	2.05×10^7	-149.05
Double-SOI	525	34 μm	200 μm	1.65×10^6	-159.99

Table 6 Parameters of MET sensing elements and calculated hydrodynamic impedance & thermal dynamic noise.

The self-noise spectrum test results for FIB, Single-SOI, Double SOI based MET seismometers compared with a commercialized CMG-6T seismometer (Guralp System Ltd.) are shown in Figure 25. Theoretically, the noise level follows the decrease of hydrodynamic impedance. Comparing with FIB process based MET device with 50, the Single-SOI based device with lower R_h has dramatically optimized the output noise level which reaches -139.32dB around 1.3Hz. However, on the contrary, results between two SOI processes indicates the Double-SOI process with lower R_h brings the higher noise level -124.39B especially around its resonant frequency 1.3Hz.

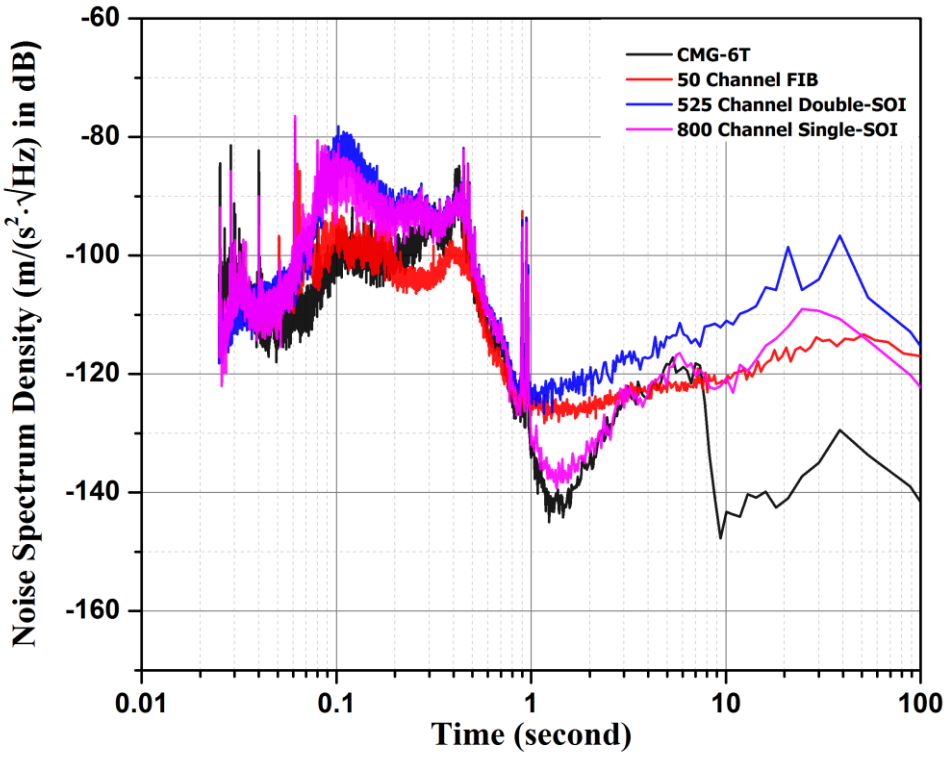

Figure 25. Noise Spectrum Density of MET seisemometers

This phenomenon can be verified by V.A.Kozlov's paper[20] in 2003. When hydrodynamic noise reaches a level of $1.5\text{-}3.0\times10^{-8}$ m/($s^2\times\sqrt{Hz}$) the turbulent fluctuations contribute becomes considerable to the total noise which is reciprocal to the hydrodynamic impedance. This phenomenon is significant to the observatories when seismic background motion is low, which indicates our design of each channel in Single-SOI process is the optimal solution. To further optimize the performance of MET seismometer for background motion detection, increasing the number of channels is the effective option based on SOI process.

Conclusion

In this chapter, three MEMS based molecular electronic transducer seismometers were studied and compared in this paper. The innovative fabrication processes based on single layer and double layer SOI wafer successfully reduced the cost and defects caused by platinum etching comparing with former designs of MET device. Those developments in MEMS fabrication process provided a breakthrough to suppress the self-noise interns of input acceleration from -124.17dB to -139.32dB, by increasing the number of channels from 50 to 800 and reforming the structure of each channel to lower hydrodynamic impedance. While double-SOI design adopts finer structure in length of each channel, in which the R_h is only 12.42 times less than double-SOI design, the dynamic analysis of noise spectrum shows a contrary result, that is 14.93dB higher at 1.3Hz. This investigated result verifies a conclusion in V.A.Kozlov's research that for those hydrodynamic noise under $1.5\text{-}3.0\times10^{-8}$ m/($s^2\times\sqrt{Hz}$), the turbulence fluctuation, which is inversely proportional R_h to begins to dominantly benefits to the total noise. In conclusion, the Single-SOI based MEMS MET seismometers presents its optimal performance in noise control by producing appropriate hydraulic conductance.

CHAPTER 5

AN IONIC-LIQUID ENHANCED

MET ACCELEROMETER

Design and Micro-Fabrication of MET Accelerometer

Traditional MET accelerometer shows in Figure 26, contains four platinum electrodes in a plane separated by LPCVD Silicon Nitride which are parallel distribution and a water-based sub-microliter electrolyte droplet encapsulated in oil consist the sensing elements.

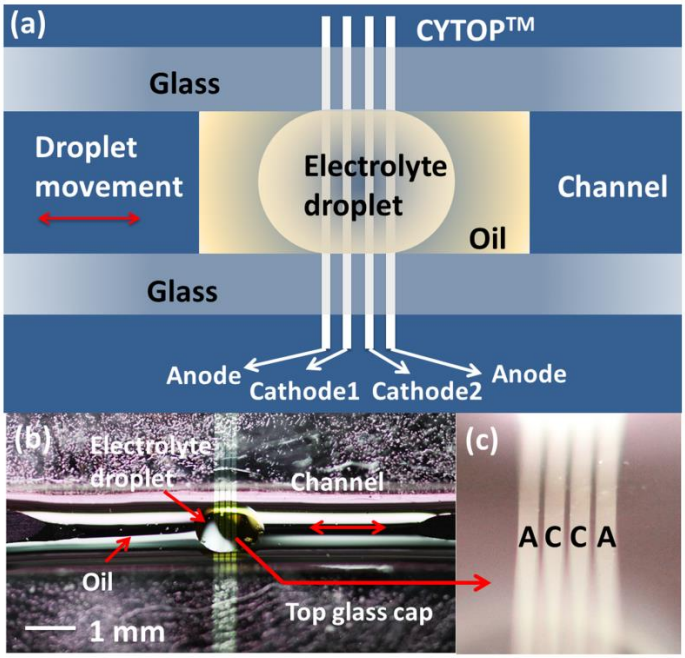

Figure 26. Overview of the electrolyte droplet-based MET accelerometer: (a) Top view schematic of the device. (b) Sensing element of the fabricated device, (c) Zoom-in view of the droplet-covered electrodes.

This part presents approaches to develop a low-frequency MET accelerometer. As a liquid based motion sensing mechanism, performances of MET correspond to both recipes of electrolyte sensing body and properties of MEMS fabricated devices. A specific design

of 3D printing improves the quality of package and decrease the cost. By replacing water based iodide solution to room temperature ionic liquid based iodide electrolyte, the properties of electrolyte based sensing mass is improved. With a specific design of 3D printing based package, the MET accelerometer consists four parts as shown in Figure 27: a silicon based sensing element with four platinum electrodes parallelly distributed on SiN insulation layer, a water-proof epoxy coated 3D printing nylon tube, two PDMS diaphragm and Ionic Liquid based iodide electrolyte.

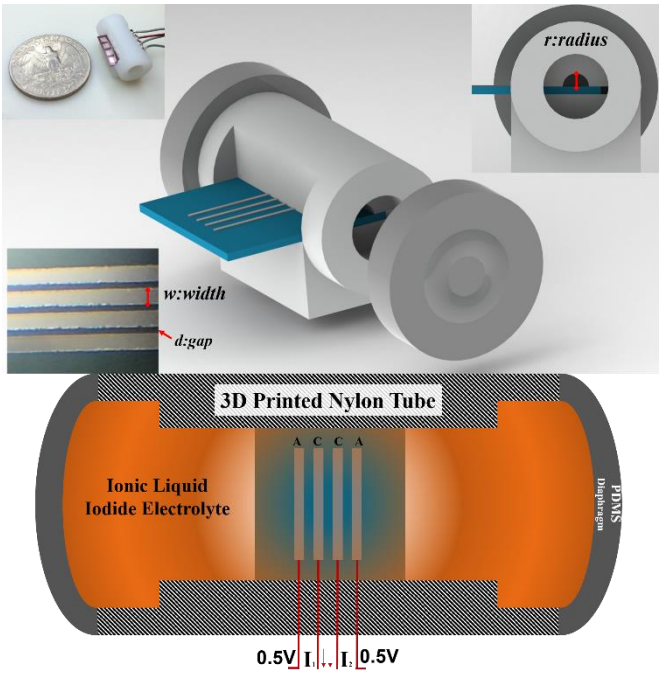

Figure 27. Schematic model and photos of MET accelerometer with 3D printing package

The core component of MET sensor is the molecular electronic sensing element. Traditional commercialized MET motion sensor uses platinum gauze as electrodes and plastic grids a dialectical spacers. Due to the lack of alignment process control resolution, those devices suffer from low reproducibility and limit optimum performance. Our work combined MET with micro electrical mechanical system (MEMS) fabrication technology and has demonstrated a novel structure containing four e-beam physical-vapor-deposited

(E-beam PVD) platinum layers with plasma-enhanced chemical-vapor-deposited (PECVD) silicon nitride (Si3N4) as an insulation layer and through-holes milled by a focus ion beam (FIB) system (Nova 200 NanoLab, FEI). [45] The simulation and experiment results of the MEMS based MET sensor indicate the micro-fabrication technology benefits the sensitivity and reproducibility more than traditional structure. However, low throughput, high cost and re-deposition issue caused by platinum etching process limits the application and provide great challenges in package. [46]

Therefore, horizontal distributed MET sensing element is developed. In standard planar microfabrication process, devices with high volume-manufacturing compatibility and low cost provide comparable performance. Figure 28 illustrates the details of fabrication processes. First, a 0.6μm layer of low pressure chemical vapor deposited (LPCVD) Silicon Nitride (Si3N4) covers a 4 inch 400μm thickness silicon wafer. Second, a photolithography process with 4μm thick positive photoresist AZ 4330 transfer the pattern of four electrodes. Then a layer of E-beam PVD deposited 20nm/200nm Ti/Pt covers the top of patterned wafer. Standard lift-off process removes the platinum covered photoresist with AZ 400T photoresist strippers at 80°C. Third, the package with channel is manufactured by selective laser sintering based additive manufacturing (3D printing) with nylon-based powder. After that, a layer of epoxy is coated on surface of printed tube to prevent the electrolyte leakage. Then, dicing the 4 inch wafer to 10mm×10mm chip and embed it in the tube with low viscosity epoxy. Afterwards, fill the tube with ionic liquid based iodide solution and seal with PDMS diaphragm. Final, we connect the electrodes to recording PCB circuit board by using conductive epoxy and 40 AWG coaxial-cable.

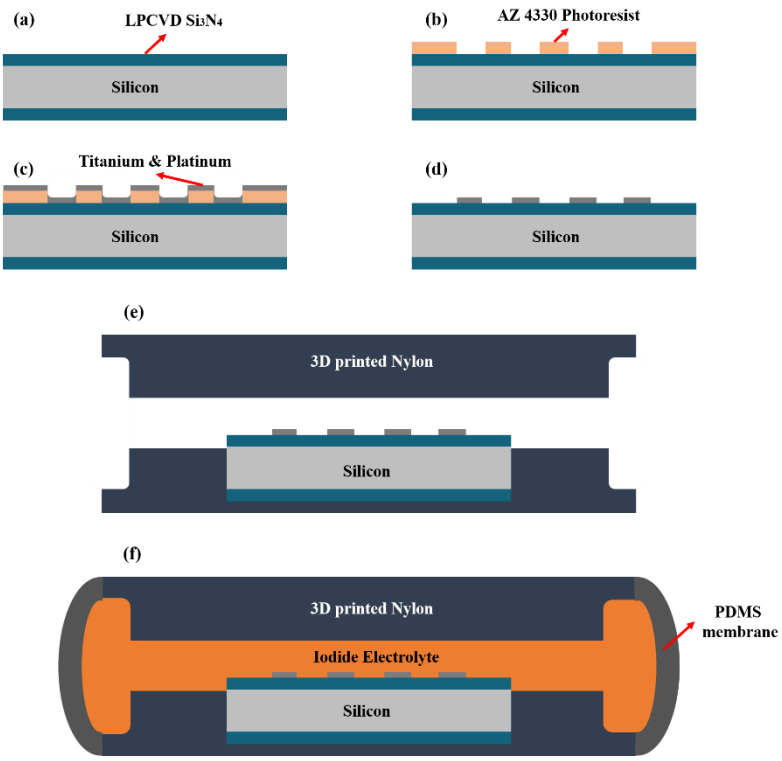

Figure 28. Microfabrication process of the ionic liquid based micro MET accelerometer, (a) silicon substrate with LPCVD Si_3N_4, (b) photolithography patterned AZ4330 photoresist, (c) e-beam evaporating PVD Ti/Pt, (d) lift-off process by AZ400T photoresist stripper, (e) embed diced chip in 3D printed Nylon tube, and (f) seal iodide electrolyte in tube with PDMS membrane.

Experimental Results and Discussion

The performance of MET accelerometer depends not only on mechanical geometry design of electrodes and channels, but also relative to the recipes of iodide electrolyte. Accordingly, the study aims at analyzing the effects from each controllable parameter to the sensitivity and noise spectrum. In this study, we design different samples for each of 4 parameters which includes: the width of ACCA electrodes, the gap between ACCA electrodes, the inner channel radius of 3D printed tube and the recipes of ILs based iodide electrolyte. The descriptions of each test samples are illustrated in Table 7. To ensure the test of each sample is under the same environment noise and amplitude of vibration, packed devices are assembled on the same platform. The whole sensing array is mounted side by the reference accelerometer and all sensing directions are vertical.

	Characteristics	Symbol	Value	# of Samples
Sensing element	Electrodes width	w	100μm*	2
			300μm	
	Electrodes gap	d	30μm*	3
			100μm	
			150μm	
Package tube	Channel inner radius	r	1.0mm*	3
			1.5mm	
			2.0mm	
* Standard parameters of MET accelerometer				

Table 7. Specifications of mechanical parameters of MET accelerometer

Study of Electrodes Width

As described in equation (12) and (13), the exposed area of electrodes affects both background current and motion current. In study of dynamic analysis in equation (16), the influence of electrode's width change depends on the change of conversion factor of electrochemical reaction. We employs tubes with 1mm radius channel and 2 sensing elements with 100µm and 300µm widths electrodes shown in Table 7, to investigate the relationship between electrodes width and sensitivity performed under 0.5Hz to 120Hz 10mg vertical vibration and noise response from 0.03Hz to 50Hz. The sensitivity and noise power spectrum results are shown in Figure 29. It demonstrates the general sensitivity follows the increasing of electrode's width especially at the resonant frequencies. Here, both two samples obtain two major resonant frequencies at 2Hz and 17Hz, but the sensitivity of w =300µm element is 2.58 times higher than w =100µm element at 2Hz (103.69V/g against 40.16V/g) and 16.89 times higher at 17Hz (58.10V/g against 3.44V/g). The noise spectrum indicates the output noise has the similar trend of sensitivity response, where the differences are about 20dB (10 times) from 0.03 to 0.5Hz, 10dB from 0.5 to 5Hz and 0dB after 15Hz.

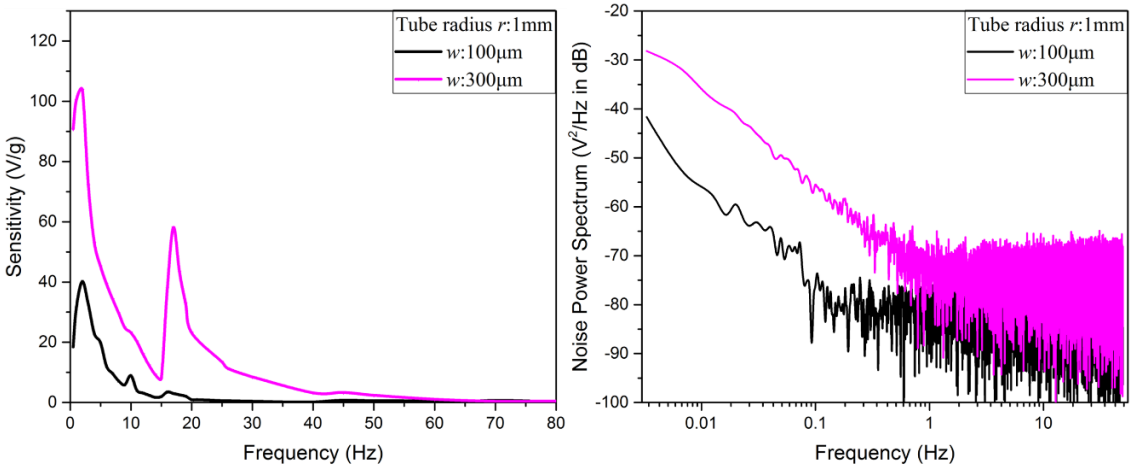

Figure 29. Device frequency magnitude response and noise power spectrum, confirming the relationship between the electrodes width and device performance.

To explain the noise from electrochemical reaction, we use the geometry self-noise model in equation (18). It is obvious that the conversion coefficient influence the noise output. In terms of the sensitivity response and noise spectrum, we can determine the resolution of w =300μm element is higher than w =100μm around resonant frequencies.

Study of electrodes spacers

Besides the diffusion coefficient D, and conversion factor C, equation (8) explains how the resonant frequency of electrochemical reaction response depends on the distance between anode-cathode pair. To verify the theory, we designed 3 devices with w =300μm, r =1mm and gaps d of 30um, 100um and 150um. Time responses under 1Hz, 5Hz and 30Hz are recorded and normalized by fast Fourier transform to frequency response. They are clearly demonstrated in Figure 30 (a)-(c). The noise power spectrum of those 3 devices are shown in Figure 30(d).

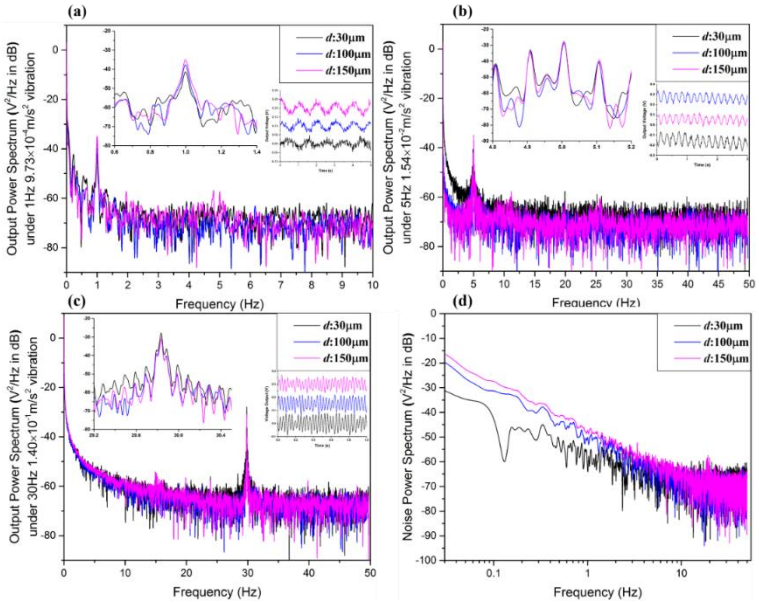

Figure 30. Output power spectrum of MET accelerometer differs in electrode's spacers (a) Test result under 1Hz vibration (b) Test result under 5Hz vibration (a) Test result under 30Hz vibration (c) Noise power spectrum without any vibration.

Table 8 illustrates the details of normalized results. At 1Hz, the resonance amplitude benefits from d=30μm more than elements with larger gaps. Results under 5Hz, shows all 3 devices have the same output amplitude, and 30Hz results present an inverse trend comparing with 1Hz results. Similarly, noise power spectrum indicates devices with smaller gap has lower noise level at low frequency range and larger noise at high frequency. 5Hz is the neutral frequency for both noise and resonance response. It obviously verified that the resonant frequency of electro-chemical reaction system has shifted to low frequency by increase the gaps from 30μm to 150μm. The results also verify the research in the previous research work from Russia's MET group. [47] The natural convection of electrolyte between two electrodes proportionally correlated to the Rayleigh number defined as:

$$R_a = \frac{g\beta\nabla c \cdot d^n}{\mu D} \tag{20}$$

Here, g is gravitational acceleration, β reflects the mass coefficient, d is the distance of gaps, n is a constant value between 3~4 under vibration at low frequency and smaller than 0 at high frequency.

specifications	*d=30μm*	*d=100μm*	*d=150μm*
Resonance amplitude (V^2/Hz in dB)			
1Hz, $9.73\times10^{-4}m/s^2$ vibration	*-39.18*	*-35.14*	*-32.47*
5Hz, $1.54\times10^{-2}m/s^2$ vibration	*-27.55*	*-27.43*	*-27.73*
30Hz, $1.40\times10^{-1}m/s^2$ vibration	*-24.28*	*-27.46*	*-27.66*
Averaged Noise amplitude (V^2/Hz in dB)			
frequency<1Hz	*-51.95*	*-43.43*	*-40.33*
1Hz<frequency<30Hz	*-67.97*	*-68.15*	*-67.55*
frequency>30Hz	*-68.08*	*-71.68*	*-72.10*

Table 8. Output amplitude and noise specifications in Study of electrodes spacers

Study of Inner Channel Radius

Figure 31 shows the sensitivity and noise response of 3 devices differed only in inner channel radius. Shown in the sensitivity response, 3 devices have the same resonant frequency ω_D of electro-chemical reaction at 17Hz which is based on the same diffusion coefficient and electrodes layout. Otherwise, resonant frequencies of fluid mechanical system are different where ω_0 is 2Hz for device of r=1mm, 17Hz for device of r=1.5mm, and 25Hz for device of r=2mm. As the resonant frequency ω_0 is relative to the stiffness coefficient k from diaphragms on sides of the channel, it can be assumed that k is proportional to $1/R_h^m$ and m is an empirical constant in MET accelerometer. The same variation is found in noise power spectrum analysis, where large channel provides 10~20dB lower noise below 2Hz and 5~10dB higher above 20Hz comparing with small channel.

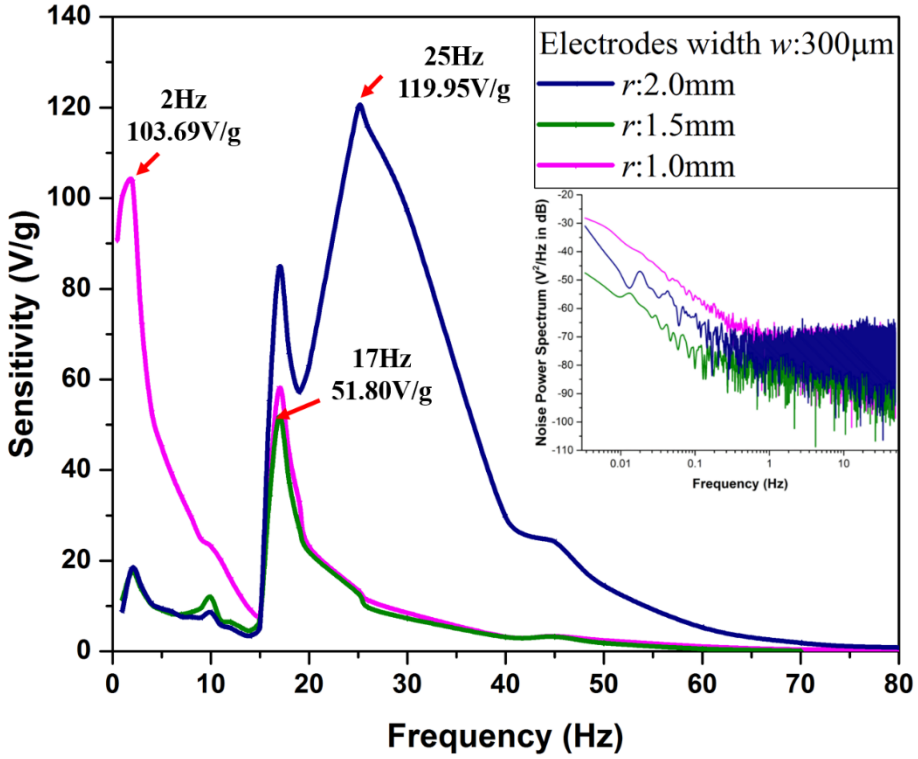

Figure 31. Sensitivity and noise power spectrum results in study of inner channel radius of 3D printing package

Improvement with Carbon Nanoparticle enhanced Ionic Liquid Electrolyte

Most previous MET motion sensors have used water with dissolved iodide salts (lithium iodide, potassium iodide, sodium iodide) as their electrolyte. However, harsh environments such as the ocean floor, the moon or other bodies in space require a sensor with wide operating temperature range, sharp resolution, high sensitivity, and long surviving time, none of which are feasible for standard water electrolytes. Improving resolution—which determines the minimal amplitude of vibration the sensor can detect—is a particularly important and challenging goal. A sharp-resolution sensor can detect subtle seismic activity which would go unnoticed by conventional sensors, allowing potentially powerful new seismological insights. Since the performance of METs relies heavily on behavior of the electrolyte, developing refined electrolytes with specific chemical properties, many of which are difficult to achieve in the same liquid, is essential. For example, electrolytes with a wide fluid temperature range tend to be highly viscous, which impedes convective motion and contributes to "self-noise,"4 or the change in signal not directly related to electrolyte movement. This obscures the electrical signal attributable to seismic motion and dulls sensor resolution. Electrolytes with increased concentrations of iodide anions generally have higher ionic conductivity and therefore improved sensor sensitivity—that is, greater change in electrical current for a given change in seismic motion. However, the same factors significantly increase self-noise resulting in no net improvement in resolution. We have found that a novel electrolyte, based on an iodide ionic liquid (IL) and enhanced with fullerene-derived carbon nanoparticles (NPs) shows excellent performance on these vital and contradictory measures.

Our electrolyte is based on 1-butyl-3-methylimidazolium iodide ([BMIM][I]). Similar to other ionic liquids, [BMIM][I] is a room-temperature liquid salt which resists crystallization due to the bulky, asymmetric BMIM cation. Our previous work on [BMIM][I]/water mixtures has found these solutions to have unusual properties compared to pure ILs or conventional salts in water, including extremely low melting temperatures (likely driven by powerful hydrogen bonding) and unusually low viscosity given this wide liquid temperature range5.The electrolyte presented here consists mainly of [BMIM][I] with some water, doped with lithium iodide (LiI) to increase iodide concentration and enhanced with phenyl-C61-butyric acid methyl ester (PCBM) fullerene nanoparticles. Without NPs, the electrolyte composition is 74 wt% [BMIM][I], 19 wt% water, and 7 wt% LiI. NPs are added at 0.001 wt%. While ILs have been used as electrolytes in various applications including dye-sensitized solar cells6 and Li-ion batteries7 and NPs have been employed in lithium sulfur batteries8, our work marks the first time either of these elements have been used in an electrolyte for an MET sensor. We find that the IL and NPs work together to improve device performance.

This novel electrolyte was tested in our own MET design, shown in Figure 1. Three electrolytes were tested: a standard MET electrolyte consisting of potassium iodide in water, the IL solution described above without NPs, and the IL solution with NPs added. A piezo-electrical seismic accelerometer (Model: 393B31 from PCBinc) with a sensitivy of 10V/g was introduced as the reference. Though this non-MET seismometer is less suitable for harsh environments and low-frequency vibrations, it is expected to have a higher sensitivity than the MET. Vibration was generated from a signal generator connected to a low-frequency shaker. Output voltage signals were recording by National

Instrument Data Acquisition and processed with Labview. The results are shown in Figure 32.

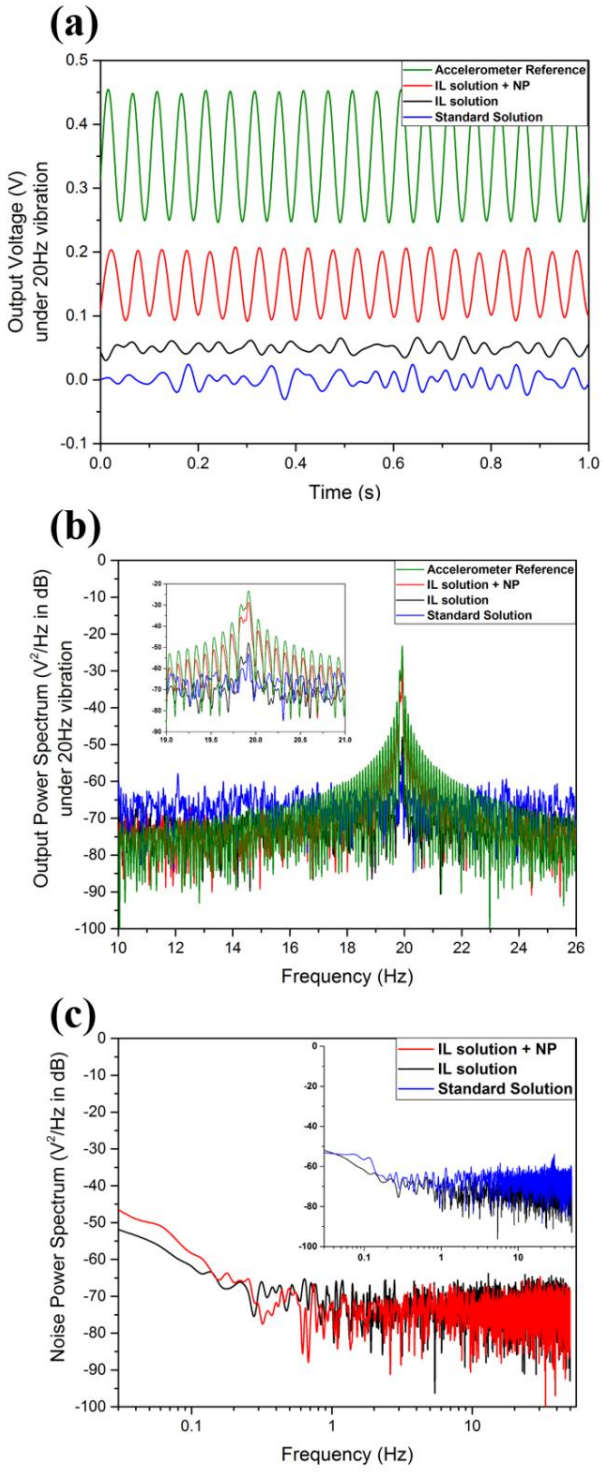

Figure 32. Test Results of MET Accelerometer with IL and Nanoparticles (a) shows the amplitude of output voltage under time domain and with a Fast Fourier Transform. (b) shows the power spectrum analysis of output voltage signal. (c) shows the noise floor power spectrum.

Output voltage (as shown in Figure 32(a) measured under 20Hz, 7.67mg sinusoidal excitation) and output power spectrum (as shown in Figure 32(b), measured across various frequencies) are both measures of sensitivity. Both measures demonstrate that the output voltage of the IL electrolyte shows some improvement over the standard electrolyte, while the IL electrolyte enhanced with NPs shows dramatic improvement. Figure32(c) shows no increase in self-noise for either IL-based electrolyte.

These results are further detailed in Table 1 where sensitivity is taken as the average offset output voltage from Figure 32(a), the noise floor is taken from Figure 32(c), and the resolution is calculated as the sensitivity over the noise floor. A smaller number for the resolution is better and indicates that the sensor can detect finer changes in vibration. The IL solution improves resolution over the standard electrolyte by 8.33x. Adding NPs to the IL solution improves resolution by a further 101x. The IL+NP electrolyte improves resolution over the standard solution by 844x.

	Sensitivity	**Noise Floor**	**Resolution**
Standard	7.29×10-3 V/g	2.05×10-4 V	2.81×10-2 g
IL	3.54×10-2 V/g	1.19×10-4 V	3.37×10-3 g
IL+NP	2.85 V/g	9.49×10-5 V	3.33×10-5 g

Table 9. Properties of MET Accelerometers with Different Electrolytes

This intriguing result means that our IL and NP electrolyte can radically improve MET performance. However, the mechanism behind this improved performance is not obvious. Since the nanoparticles do not raise the noise floor, they cannot be increasing sensitivity simply by increasing conductivity. A more complex explanation, taking into account the unique chemical properties of the electrolyte, is needed.

To form a preliminary theory of this mechanism, a simple molecular dynamics (MD) simulation was performed using GROMACS simulation tools9. A fullerene nanoparticle was simulated within a mixture of water and [BMIM][I], using the model developed in our previous simulation work. [40] Figure 33 shows a radial distribution function (RDF) diagram derived from this simulation, as well as snapshots of the simulation before equilibration and after five nanoseconds of simulation at constant temperature and pressure. The simulation clearly shows the relatively-hydrophobic BMIM anions gathering around the hydrophobic fullerene NP. The iodide cations tend to gather farther from the NP. The IL effectively forms a double-layered solvation shell around the particle.

From this observation, we have developed a theory. The relatively large and heavy NPs effectively "anchor" IL molecules. This limits diffusion while the bulk liquid is inert, which limits self-noise. The NPs move along with the convective motion of the bulk fluid, dragging IL molecules along with them. Meanwhile, the NPs draw the BMIM molecules in, leaving the iodide atoms relatively open. The iodide (and, presumably triiodide complexes) have easier access to the electrodes without bulky BMIM molecules in their way. This encourages timely redox reactions at the electrodes and increases sensitivity. Strategies for further increasing sensitivity, therefore, might include experimenting with different nanoparticles. Smaller or larger particles with differing surface areas may affect

the ordering of IL molecules around the particle surface. So might particles with different functional groups attached to adjust hydrophobicity and charge. The complex chemical interactions between nanoparticles, ionic liquid, and water create promising opportunities for the development of improved electrolytes and MET sensors capable of measuring increasingly subtle changes in seismic motion, with promising implications for seismic research.

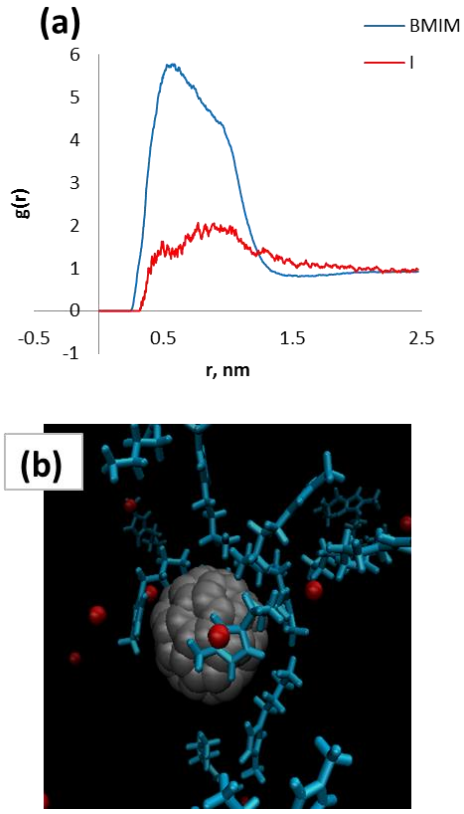

Figure 33. Simulation Results of Carbon Nanoparticle in BMIM (a) shows the radial distribution function of the IL cation and anion around the nanoparticle. (b) shows a snapshot from the simulation, illustrating the way BMIM molecules are attracted to the NP surface.

Conclusion

In conclusion, the effects of each electrochemical and mechanical parameter to the dynamic characteristics of ionic liquid based MET accelerometer was studied in this paper. In terms of the experiment results, devices with large electrodes width, large spacers, small channel radius, high density and small viscosity electrolyte can optimize the low frequency < 10Hz response of MET accelerometer. With the improvement of package by 3D printing technology and ionic liquid based iodide solution, the sensitivity of MET accelerometer with w=300μm, d=30μm, r=1mm and standard IL based iodide electrolyte, reach 103.69V/g at 2Hz with the averaged noise around 5.40×10^{-4}V, in terms of 5.25μg/√Hz resolution. With the improvement of carbon nanoparticles enhanced ionic liquid based iodide electrolyte, the resolution can be improved by 101 times higher than the standard water based electrolyte.

CHAPTER 6

BATTERY ACCELEROMETER

Design and 3-D Printing enhanced Fabrication Process

As described in the previous chapters, traditional MET sensor includes four electrodes with same metal material such platinum. As the results, those sensors require external source of power to operate which is kind of active motion sensor and the output current needs one stage of trans-impedance amplifier to convert to voltage signal which import extra current noise from op-amplifier. Most passive commercialized inertial motion sensors are based on piezo-electrical operation principle or electro-magnetic component. Although, those sensors use energy harvesting technology to detect inertial motion with relatively high resolution, the efficiency of energy converting is limited by the size of mass-spring system. Inspired by the operation principle of traditional battery, Galvanic Cell, we develop a novel passive inertial motion sensor by combining Cu-Zn battery and MET technology named “Battery Accelerometer”.

As shown in Figure 34, Battery Accelerometer contains one 500μm thick copper plate and one 500μm zinc plate with 23 small channels with 1mm diameter, one polymer package with same layout of 1mm channel by photosensitive 3D printing polymer material and two PDMS membrane for the sealing. When filling with CuI2 electrolyte solution there will be an electrical potential between copper (anode) and zinc (cathode) plate. The output voltage signal is filled by high pass filter and made a difference by an instrumental differential amplifier with gain of 100V/V.

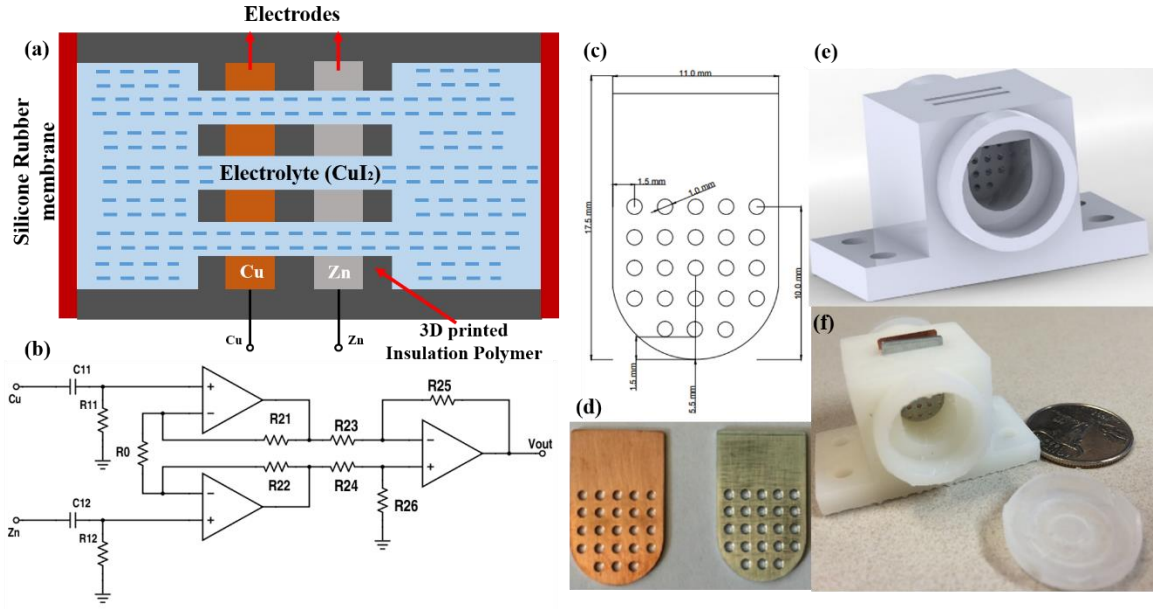

Figure 34. Schematic of Battery Accelerometer cell, (a) Drawing layout of whole system, (b) Schematic of circuits design (c) Cross section of Battery Accelerometer sensing element (d) Photo of drilled and diced copper and zinc plate (e) 3D model for 3D printing package (f) the whole assembled system.

The cell is 32 mm long, 24 mm wide. Two rectangular openings on the top are for inserting electrodes. The copper and zinc electrodes are both 11 mm wide, 17.5 mm long and 1mm thick. And holes of 1 mm in diameter are drilled on electrodes to allow the motion of electrolyte in the cell. Between the two electrodes is a 2 mm thick dielectric polymer sheet to keep two electrodes away. The polymer sheet is also drilled at the same positions as the electrodes. After mounting electrodes, the gap between electrodes and the cell is sealed with Epoxy to ensure no leakage. The MET accelerometer cell is sealed with high flexible silicone rubber on both portholes and is filled with saturated CuI_2 solution.

Experimental Results and Discussion

Schematic experimental setup is shown in the Figure 35, data collecting part is isolated from the vibration area in order to cut out distraction. With Data Acquisition Card, vibration data can be recorded by the Labview and sensitivity and resolution of the MET sensor can be calculated according to the time domain chart with fast Fourier transform (FFT) tool. PCB 393B31 model piezoelectric based accelerometer is employed as an acceleration reference with working frequency range from 0.1Hz to 200Hz, resolution 0.1μG/√Hz and sensitivity of 10V/G. The electro-magnetic shaker is controlled by sinusoidal signal generator and power amplifier. The test range is from 5Hz to 100Hz.

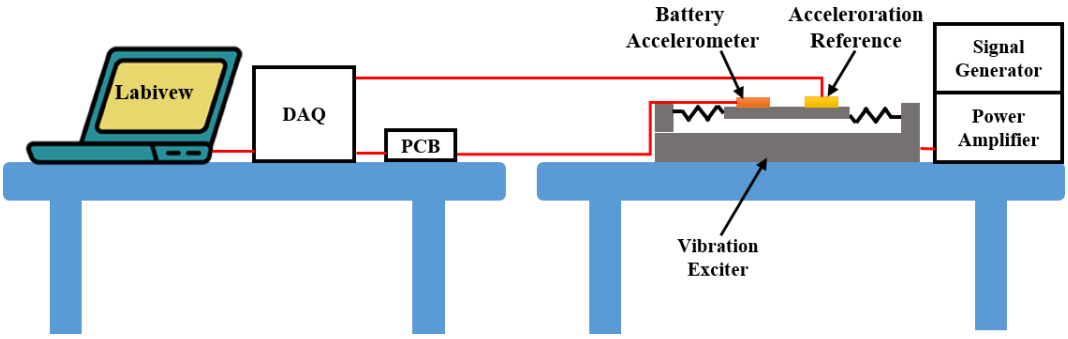

Figure 35 schematic of test setup for Battery Accelerometer

Figure 36 presents the time domain results of test under 40Hz 0.95G sinusoidal vibration. It is obvious that our battery accelerometer has 5 times less sensitive than the reference one at 40Hz with 1/4 period phase shift.

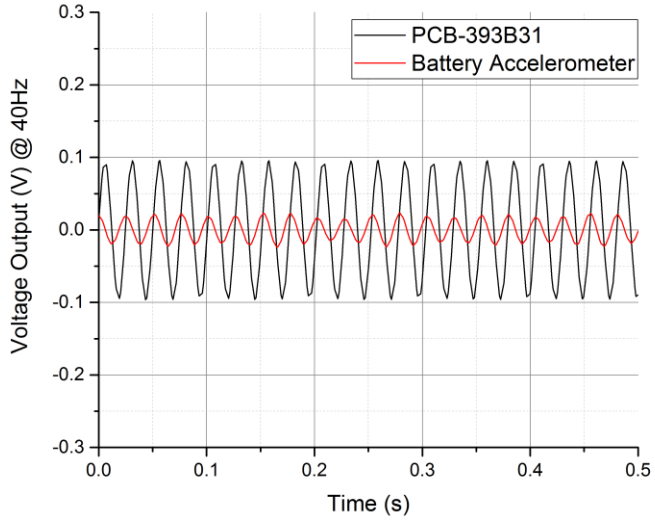

Figure 36. Comparison of time domain results of PCB 393B31 piezoelectric accelerometer and Battery Accelerometer

By transfer the above results with FFT, Figure 37 presents the frequency domain results of 40Hz 0.9g vibration. The result indicates that harmonic resonant response of Battery Accelerometer is less than the reference one.

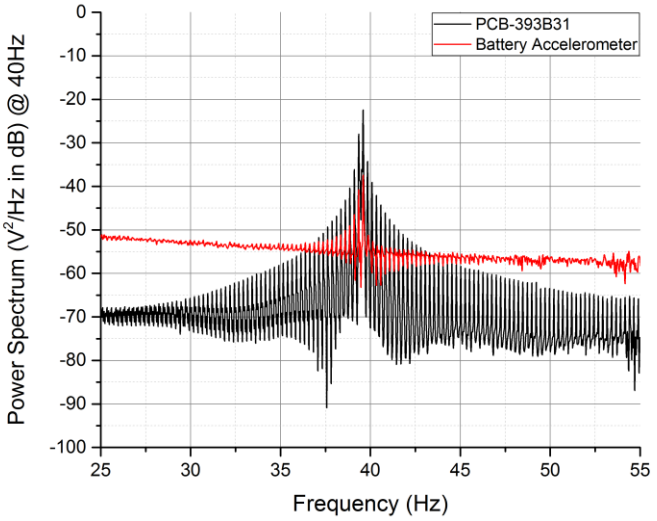

Figure 37. Frequency response of Battery Accelerometer under 40Hz vibration

Figure 38 shows the amplitude linearity of Battery Accelerometer under 40Hz within the vibration range from 1mg to 16mg. By tuning the gain, the MET accelerometer shows a good linearity sensitivity at 40Hz.

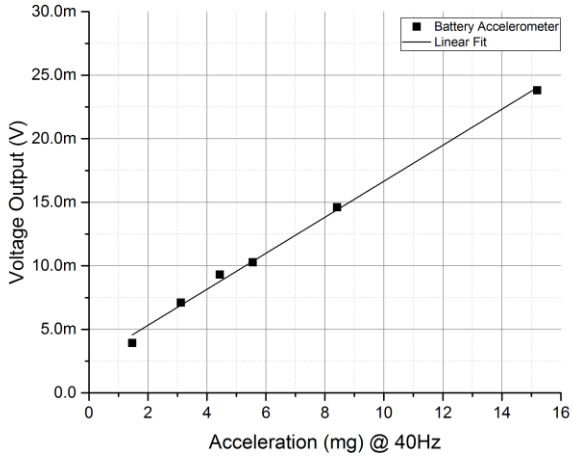

Figure 38. Linearity test results for Battery Accelerometer

As shown in Figure 39, the frequency response of sensitivity of the MET accelerometer shows a peak sensitivity 10.4 V/G at its resonant frequency 18Hz and an almost flat response between 31Hz to 60Hz.

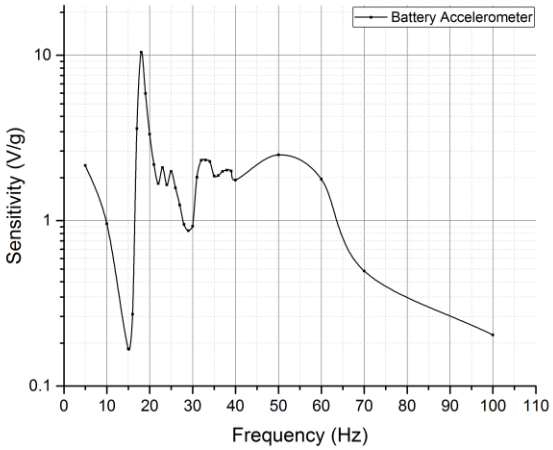

Figure 39. The frequency response of Battery Accelerometer.

Figure 40 shows the noise power spectrum of the whole system. At 40Hz, the amplitude of noise floor is -85dB which is 3×10^{-6}V. By divided by the sensitivity of 1.9V/G at 40Hz. The resolution at 40Hz can reach 1.57μg.

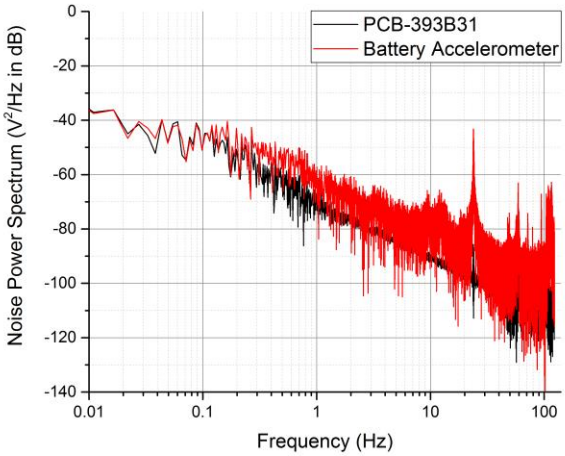

Figure 40. The noise power spectrum of Battery Accelerometer

Conclusion

In conclusion, Battery Accelerometer provides an idea which use electro-chemical self-powered energy and the electrical potential change caused by ions concentration variation followed by the electrolyte flow in the channel to sense the external acceleration. With the development of package by 3D printing technology and dialectical epoxy, our battery accelerometer shows good performance at frequency range of 5Hz to 100Hz with the peak sensitivity of 10.6V/g at 18Hz and resolution around 1.57μg. The linearity test shows the device has good linearity from 1mg to 16mg vibration.

CHAPTER 7

AN IONIC-LIQUID ELECTROLYTE BASED MET INCLINOMETER

Design and Micro-Fabrication Process

Inclinometer is a gravity sensitive device which is capable of measuring the tilting angle. Small size, high resolution and small constant time are important factors for inclinometer design in a broad range of disciplines including consumer electronic devices and earth and space exploration. Developing high quality of inclinometer with high resolution and reliability under harsh environment detection is important for market needs. Micro solid-state tilt sensors have been developed [48-50] with a mass-spring system consisting of a suspended proof mass. However, these sensors can hardly obtain linear output as the limitation of solid mass spring system. Additionally, planet exploration requires sensors can survive in broad temperature range which traditional solid-state and liquid based inclinometer are difficult to achieve.

Apposed to solid-state motion sensing element, Molecular Electronic Transducer (MET) based motion sensor is sensitive to the motion of liquid flow relative to fixed electrodes. As only dynamic acceleration cause continuous liquid flow, one of the advantage of MET motion sensor is that its performance does not vary with installation angle and gravity. However, even by optimizing the geometry and sensing the instant velocity peak, the MET motion mechanism can only estimate the static acceleration. [33] This characteristic limits the MET motion sensor in application of incline angle detection.

With the development of MET technology, the bias current of the system has been found linearly relative to the covered electrodes area and this letter introduces an

innovation design for tilt angle sensing called MET inclinometer. As shown in Figure 41, a Polydimethylsiloxane (PDMS) mold with macro size channel was bonded on the MET sensing element with microelectromechanical systems (MEMS) microfabrication. Two platinum swirl shaped electrodes widths change with tilt angle.

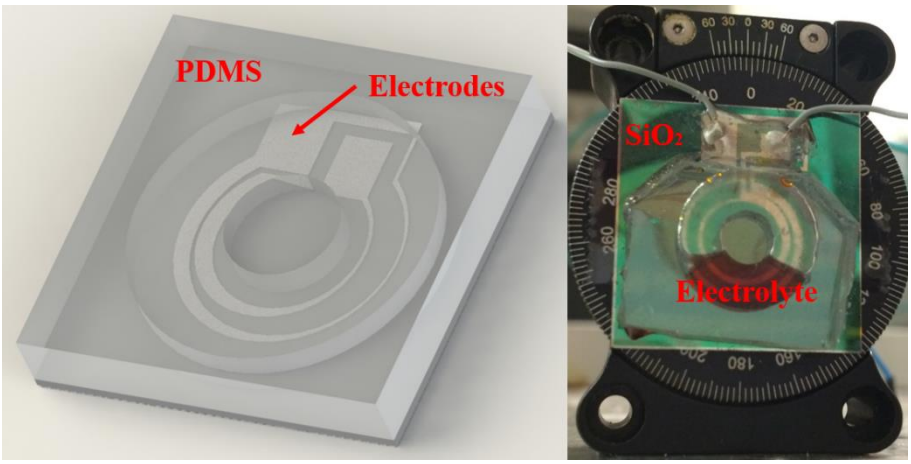

Figure 41. Overview of the MET inclinometer with ionic liquid based electrolyte as sensing body

Concentrated lithium iodide (Li2I) was dissolved in the bmim a non-water-soluble ionic liquid as the sensing body with CYTOP material an amorphous fluoropolymer to decrease the surface tension.

As shown in the Figure 42, the fabrication process starts with a polished silicon wafer with 600nm SiO2 layer on the top side. Two E-beam PVD 10nm Ti/ 200nm Pt swirl shaped electrodes are deposited on top of SiO2 layer by lift-off process. Secondly, a PMDS ring shaped channel is made with ring shape magnet. Then, oxygen plasma is treated on the surface of PDMS channel which active the surface to bond with SiO2. The next step is to bond the PDMS channel with fabricated device on top of SiO2.With the plasma treatment method, the bond could avoid leakage under high pressure and high shock which is

introduced in the previous paper. [34] The final step is to inject ionic liquid based electrolyte with 1% CYTOP (hydrophobic coating).

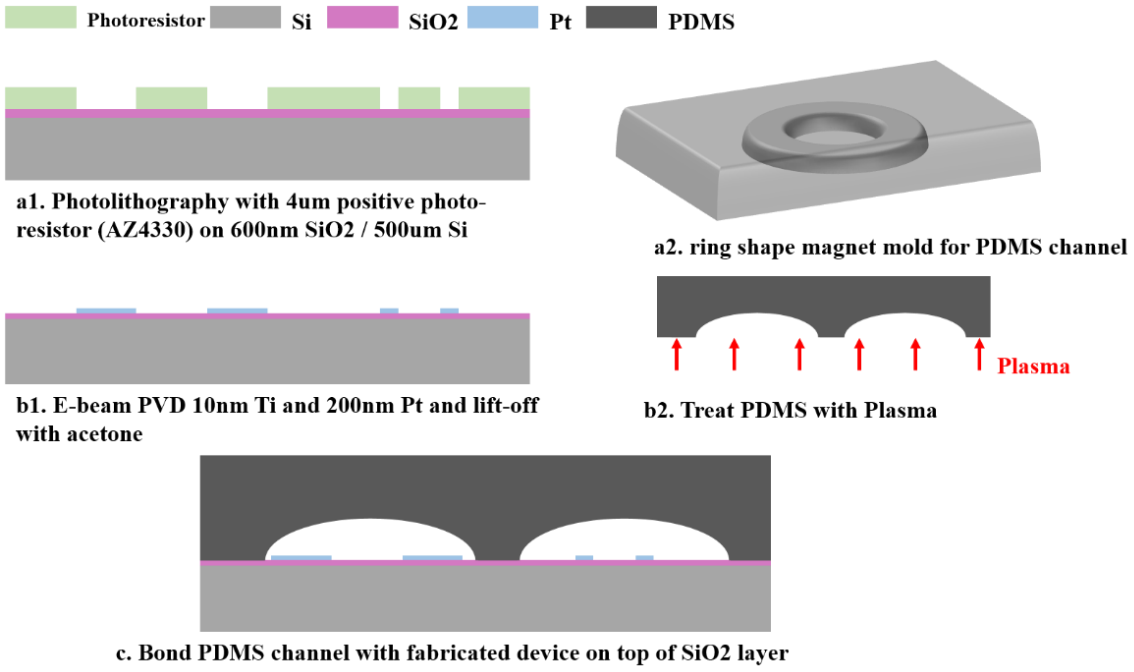

Figure 42. Microfabrication Process of MET inclinometer

As the droplet motion and electrical signal depends on both the PDMS channel and platinum electrodes layout, different device geometries and PDMS channels are designed with the same process. Based on the equation (12), the output current depends on the surface area of electrodes, two swirl shaped electrodes are designed as shown in Figure 20 to change the surface area with the change of tilting angle. The output current is proportional to the surface area of contact electrodes, so we can get the surface area:

$$\begin{cases} dS_1 = \dfrac{d\theta}{2\pi}\pi(R_1^2 - R_2^2) \\ R_2 = (R_{2\max} - R_{2\min})\dfrac{\sqrt{\alpha}}{2\pi} \\ dS_2 = \dfrac{d\theta}{2\pi}\pi(R_3^2 - R_4^2) \\ R_3 = (R_{3\max} - R_{3\min})\dfrac{\sqrt{\alpha}}{2\pi} \end{cases} \tag{21}$$

where the $d\theta$ is the angle the solution covered, dS is the covered area and α is the tilt angle. According to equation (1) and (2), the output current can be explained as:

$$I = Dq\oint_{\theta}\left((\nabla c,\mathbf{n})\left[\frac{\pi(R_1^2-R_2^2)}{2\pi}+\frac{\pi(R_3^2-R_4^2)}{2\pi}\right]d\theta\right)\propto\alpha \tag{22}$$

where the current is proportional to tilt angle.

Experimental Results and Discussion

In order to validate with the experiment, two samples with different device geometry and electrolyte volume were designed with the following parameters in Table 10.

Parameters (unit in mm)	Sample 1	Sample 2	Sample 3	Sample 4
PDMS channel width	4.5	4.5	4.5	3.2
PDMS channel height	2.5	2.5	2.5	1.5
Electrodes max width	1.0	1.0	1.0	1.0
Electrodes min width	0.2	0.2	0.2	0.2
Outer swirl radius	6.1	6.1	6.1	4.1
Inner swirl radius	4.0	4.0	4.0	2.0
Electrolyte covered angle	132°	132°	206°	30.6°
Applied voltage	0.5V	1.0V	0.5V	0.5V

Table 10. Parameters of sample 1, 2, 3, 4 MET inclinometers

As shown in the Figure 43, four samples are installed on optical rotation platform vertically, connecting with trans-impedance amplifier which amplified the output current 1000 times to voltage signal. The output voltage signals were recorded by USB-6289 data acquisition from National Instrument and analyzed by Labview. Both the average voltage data and variation region are recorded to indicate the resolution and reliability.

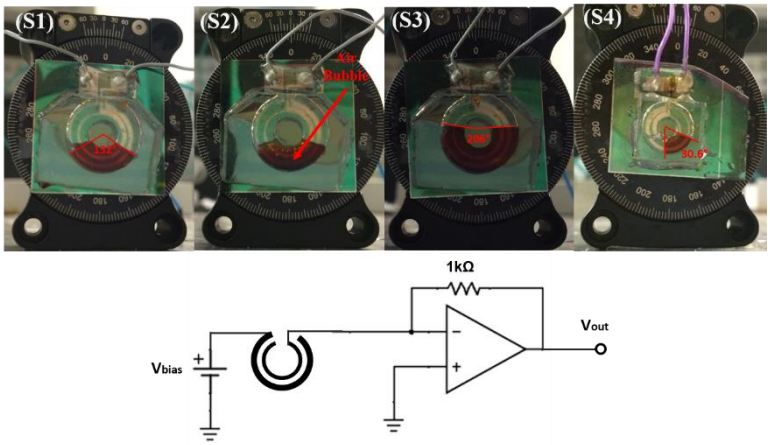

Figure 43. Test setup of Sample 1-4 with various electrodes layout, applied voltage, volume of electrolyte and the record circuit design.

As shown in the Figure 44, the output is obtained voltage output of S1 and S4 from -

90° to 90° tilt angle. The plot indicates sensitivity of 0.102mV/degree and resolution of 0.184 degree for Sample 1 and sensitivity of 0.019mV/degree and resolution of 0.998 degree for Sample 4.

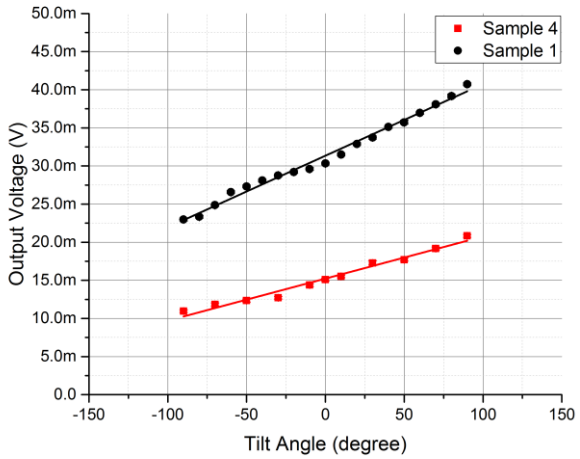

Figure 44. Output voltage of Sample 1 and Sample 4 as a function of inclination angle.

Figure 45 shows the time constant between 0 to -90° of Sample 1 and Sample 4. The Sample 1 has 5 times less time constant of 40s less than Sample 4.

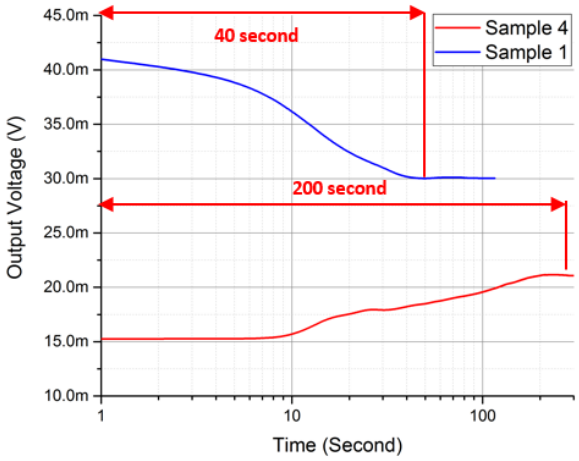

Figure 45. Response time of the Sample 1 and Sample 4 between 0° and -90°

When applying higher input voltage and larger volume of electrolyte in Sample 2 and

Sample 3, the time response shows the output current didn't change with inclination angle but very sensitive response to the initial acceleration shown in the Figure 46.

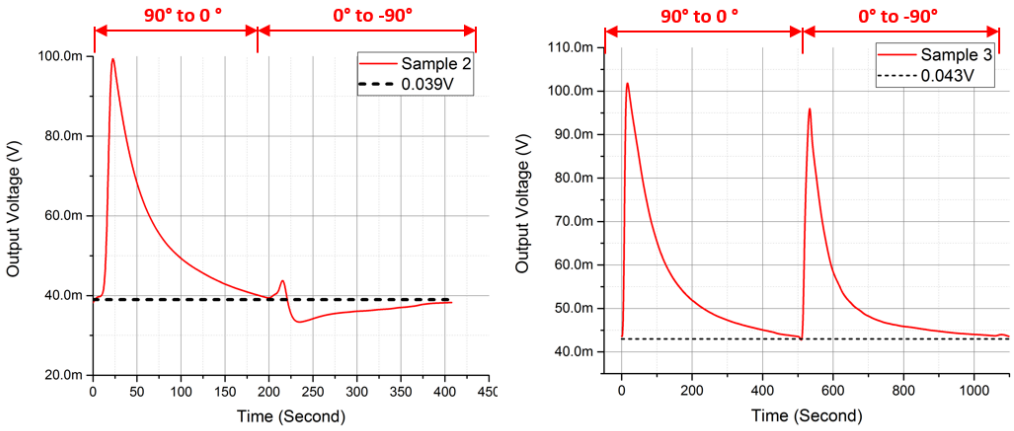

Figure 46. Response time of Sample 2 and Sample 3 which indicates the current is saturated and don't change with the inclination angle.

Conclusion

In conclusion, the design of Molecular Electronic Transducer inclinometer which used ionic liquid based LiI droplet as the sensing body shows good performance between -90° to 90° inclination angle. With combined the MET and MEMS technology, the fabrication process is less complicated than traditional solid-state inclinometer design. Additionally, the Bmim ionic liquids based solution can survive in wide temperature range which improves the reliability in harsh environment exploration. With better controls of electrolyte volume, device geometry and voltage supply, the sensitivity can reach 0.102mV/degree with resolution of 0.184 degree and time constant of 40s from 90° to 0°. This innovation broad the application of MET technology and its advantages in earth and space exploration.

REFERENCES

[1] J. Milne, *Earthquakes and other earth movements* vol. 56: D. Appleton, 1886.

[2] H.-S. Yan, *Reconstruction designs of lost ancient Chinese machinery* vol. 3: Springer Science & Business Media, 2007.

[3] J. Dewey and P. Byerly, "The early history of seismometry (to 1900)," *Bulletin of the Seismological Society of America,* vol. 59, pp. 183-227, 1969.

[4] R. Musson, "A history of British seismology," *Bulletin of Earthquake Engineering,* vol. 11, pp. 715-861, 2013.

[5] J. Milne, *Seismology* vol. 85: K. Paul, Trench, Trübner, 1908.

[6] W. Lee, H. Kanamori, P. Jennings, and C. Kisslinger, "Earthquake and Engineering Seismology," *Part A (Academic, New York, 2002)*, pp. 269-281, 2002.

[7] K. S. Jaiswal, D. Bausch, R. Chen, J. Bouabid, and H. Seligson, "Estimating annualized earthquake losses for the conterminous United States," *Earthquake Spectra,* vol. 31, pp. S221-S243, 2015.

[8] B. F. Howell Jr, *An introduction to seismological research: history and development*: Cambridge University Press, 2005.

[9] C. F. Richter, "An instrumental earthquake magnitude scale," *Bulletin of the Seismological Society of America,* vol. 25, pp. 1-32, 1935.

[10] P. Wiejacz, "Instrumentation in Earthquake Seismology by Jens Havskov and Gerardo Alguacil," *Pure and Applied Geophysics,* vol. 166, pp. 2099-2100, 2009.

[11] N. Mori, T. Takahashi, T. Yasuda, and H. Yanagisawa, "Survey of 2011 Tohoku earthquake tsunami inundation and run-up," *Geophysical Research Letters,* vol. 38, 2011.

[12] G. Sutton, W. McDonald, D. Prentiss, and S. Thanos, "Ocean-bottom seismic observatories," *Proceedings of the IEEE,* vol. 53, pp. 1909-1921, 1965.

[13] G. V. Latham, M. Ewing, F. Press, G. Sutton, J. Dorman, Y. Nakamura, *et al.*, "Passive seismic experiment," *Science,* vol. 167, pp. 455-457, 1970.

[14] Y. Nakamura, G. V. Latham, and H. J. Dorman, "Apollo lunar seismic experiment-final summary," in *Lunar and Planetary Science Conference Proceedings*, 1982, p. 117.

[15] W. Banerdt, S. Smrekar, P. Lognonné, T. Spohn, S. Asmar, D. Banfield, *et al.*, "InSight: a discovery mission to explore the interior of Mars," in *Lunar and Planetary Science Conference*, 2013, p. 1915.

[16] D. Tsuji and N. Teanby, "Seismic detectability of meteorite impacts on Europa," in *EGU General Assembly Conference Abstracts*, 2016, p. 1352.

[17] E. Wielandt, "Common Seismic Sensors," *New Manual of Seismological Observatory Practice 2 (NMSOP-2)*, p. 26, 2012.

[18] M. Lemkin and B. E. Boser, "A three-axis micromachined accelerometer with a CMOS position-sense interface and digital offset-trim electronics," *IEEE Journal of solid-state circuits*, vol. 34, pp. 456-468, 1999.

[19] C. Lu, M. Lemkin, and B. E. Boser, "A monolithic surface micromachined accelerometer with digital output," *IEEE Journal of Solid-State Circuits*, vol. 30, pp. 1367-1373, 1995.

[20] S.-H. Tseng, M. S. Lu, P.-C. Wu, Y.-C. Teng, H.-H. Tsai, and Y.-Z. Juang, "Implementation of a monolithic capacitive accelerometer in a wafer-level 0.18 μm CMOS MEMS process," *Journal of Micromechanics and Microengineering*, vol. 22, p. 055010, 2012.

[21] J. Wu, G. K. Fedder, and L. R. Carley, "A low-noise low-offset capacitive sensing amplifier for a 50-$\mu g/\sqrt{Hz}$ monolithic CMOS MEMS accelerometer," *IEEE Journal of Solid-State Circuits*, vol. 39, pp. 722-730, 2004.

[22] J. Chae, H. Kulah, and K. Najafi, "A monolithic three-axis micro-g micromachined silicon capacitive accelerometer," *Journal of Microelectromechanical systems*, vol. 14, pp. 235-242, 2005.

[23] H. Qu, D. Fang, and H. Xie, "A monolithic CMOS-MEMS 3-axis accelerometer with a low-noise, low-power dual-chopper amplifier," *IEEE Sensors journal*, vol. 8, pp. 1511-1518, 2008.

[24] C.-M. Sun, M.-H. Tsai, Y.-C. Liu, and W. Fang, "Implementation of a monolithic single proof-mass tri-axis accelerometer using CMOS-MEMS technique," *IEEE Transactions on Electron devices*, vol. 57, pp. 1670-1679, 2010.

[25] H. Huang, "Molecular Electronic Transducer-Based Seismometer and Accelerometer Fabricated With Micro-Electro-Mechanical Systems Techniques," Arizona State University, 2014.

[26] A. Wittenborn, "Analysis of a logarithmic solion pressure detector," *The Journal of the Acoustical Society of America*, vol. 30, pp. 683-683, 1958.

[27] N. O. Laboratory, H. B. Reed, and R. H. Hurd, *Solion: Principles of Electrochemistry and Low-power Electrochemical Devices*: U.S. Office of Technical Services, 1958.

[28] R. Hurd and W. Jordan, "The principles of the solion," *Platinum Metals Review,* vol. 4, pp. 42-47, 1960.

[29] J. L. Collins, W. C. Richie, and G. E. English, "Solion infrasonic microphone," *The Journal of the Acoustical Society of America,* vol. 36, pp. 1283-1287, 1964.

[30] R. M. Hurd and R. N. Lane, "Principles of Very Low Power Electrochemical Control Devices," in *J. Electrochem. Soc.* vol. 104, ed: The Electrochemical Society, 1957, pp. 727-730.

[31] G. E. English and C. W. Larkam, "Response characteristics of polarized cathode solion linear acoustic transducers," in *The Journal of the Acoustical Society of America* vol. 58, ed: Acoustical Society of America, 1975, pp. 266-272.

[32] V. Kozlov, A. Korshak, and N. PET'KIN, "Theory of diffusion-type transducers for ultralow electrolyte flow rates," *Soviet electrochemistry,* vol. 27, pp. 16-21, 1991.

[33] V. Kozlov and D. Terent'ev, "Transfer function of a diffusion transducer at frequencies exceeding the thermodynamic frequency," *Russian journal of electrochemistry,* vol. 39, pp. 401-406, 2003.

[34] I. Zakharov and V. Kozlov, "Stationary convective diffusion and nonlinear effects in an electrochemical transducer," *Russian journal of electrochemistry,* vol. 39, pp. 397-400, 2003.

[35] M. Usher, "Developments in seismometry," *Journal of Physics E: Scientific Instruments,* vol. 6, p. 501, 1973.

[36] M. Galiński, A. Lewandowski, and I. Stępniak, "Ionic liquids as electrolytes," *Electrochimica Acta,* vol. 51, pp. 5567-5580, 2006.

[37] A. E. Visser, N. J. Bridges, and R. D. Rogers, *Ionic Liquids: Science and Applications* vol. 1117: ACS Publications, 2012.

[38] S. Gabriel and J. Weiner, "Ueber einige abkömmlinge des propylamins," *Berichte der deutschen chemischen Gesellschaft,* vol. 21, pp. 2669-2679, 1888.

[39] J. S. Wilkes, "Ionic liquids in perspective: the past with an eye toward the industrial future," *ChemInform,* vol. 33, pp. 238-238, 2002.

[40] S. D. Nickerson, E. M. Nofen, H. Chen, M. Ngan, B. Shindel, H. Yu, *et al.*, "A combined experimental and molecular dynamics study of iodide-based ionic liquid

and water mixtures," *The Journal of Physical Chemistry B*, vol. 119, pp. 8764-8772, 2015.

[41] H. Huang, B. Carande, R. Tang, J. Oiler, Z. Dmitriy, A. Vadim, *et al.*, "Development of a micro seismometer based on molecular electronic transducer technology for planetary exploration," in *Micro Electro Mechanical Systems (MEMS), 2013 IEEE 26th International Conference on*, 2013, pp. 629-632.

[42] V. Kozlov, V. Agafonov, J. Bindler, and A. Vishnyakov, "Small, low-power, low-cost sensors for personal navigation and stabilization systems," in *Proceedings of the 2006 National Technical Meeting of The Institute of Navigation, Monterey, CA, USA*, 2006, pp. 18-20.

[43] V. M. Agafonov and D. L. Zaitsev, "Convective noise in molecular electronic transducers of diffusion type," in *Tech. Phys.* vol. 55, ed: SP MAIK Nauka/Interperiodica, 2010, pp. 130-136.

[44] H. Huang, V. Agafonov, and H. Yu, "Molecular Electric Transducers as Motion Sensors: A Review," in *Sensors 2011, Vol. 11, Pages 638-660* vol. 13, ed: Multidisciplinary Digital Publishing Institute, 2013, pp. 4581-4597.

[45] H. Huang, B. Carande, R. Tang, J. Oiler, Z. Dmitriy, A. Vadim, *et al.*, "Development of a micro seismometer based on molecular electronic transducer technology for planetary exploration," in *2013 IEEE 26th International Conference on Micro Electro Mechanical Systems (MEMS)*, ed: IEEE, 2013, pp. 629-632.

[46] M. Liang, H. Huang, V. Agafonov, R. Tang, R. Han, and H. Yu, "Molecular electronic transducer based planetary seismometer with new fabrication process," in *2016 IEEE 29th International Conference on Micro Electro Mechanical Systems (MEMS)*, ed: IEEE, 2016, pp. 986-989.

[47] V. Kozlov and M. Safonov, "Self-noise of molecular electronic transducers," *Technical Physics*, vol. 48, pp. 1579-1582, 2003.

[48] H. Jung, C. J. Kim, and S. H. Kong, "An optimized MEMS-based electrolytic tilt sensor," *Sensors and Actuators A: Physical*, vol. 139, pp. 23-30, 2007.

[49] L. Tang, K. Zhang, S. Chen, G. Zhang, and G. Liu, "MEMS inclinometer based on a novel piezoresistor structure," *Microelectronics Journal*, vol. 40, pp. 78-82, 2009.

[50] S. Billat, H. Glosch, M. Kunze, F. Hedrich, J. Frech, J. Auber, *et al.*, "Micromachined inclinometer with high sensitivity and very good stability," *Sensors and Actuators A: Physical*, vol. 97, pp. 125-130, 2002.

APPENDIX A

FABRICATION PROCESS FLOW

A.1 Micro-Fabrication Process for Single-SOI based MET Seismometer

Step	Process Name	Description	Material	Parameters
1	Photolithography #1	Patterning backside for DRIE	Photoresist AZ4620	2000rpm, 10 µm
2	Deep RIE #1	Thin down Si Substrate from 300µm to 150µm by DRIE	SiO_2, Si	0.3 µm/cycle
3	Clean Photoresist	Clean AZ4620 with acetone and O_2 plasma	Acetone	200W, 20min
4	Photolithography #2	Patterning device layer of SOI wafer in 800 circles	Photoresist AZ4620	2000rpm, 10 µm
5	Deep RIE #2	Etching Si device 150µm until SiO_2 box layer exposed	SiO_2, Si	0.3 µm/cycle
6	HF wet Etching	Remove SiO_2 on SOI layer and form 2 µm undercut by HF wet etching	SiO2	2 µm SiO2 and 2 µm under cut
7	Deep RIE #3	Etching through all Si Substrate 150µm	SiO_2, Si	0.3 µm/cycle
8	Clean Photoresist	Clean AZ4620 with acetone and O_2 plasma	Acetone	200W, 20min
9	E-beam Evaporation Pt/Ti deposit	Deposit Pt/Ti on both side and side wall	Pt/Ti, Si	0.2 µm Pt
10	LPCVD parylene	Coating 20 µm parylene on top side	Parylene, Si	10 g Parylene
11	Photolithography #3	Pattern parylene for RIE	PR AZ 4620	1500rpm, 15 µm
12	Parylene RIE etching	RIE parylene by O_2 Plasma	Parylene	20 µm 200W
13	Wafer Bonding	Bonding two wafers on parylene coated layer	Parylene	230ºC,1000N, 30min

A.2 Micro-Fabrication Process for Double-SOI based MET Seismometer

Step	Process Name	Description	Material	Parameters
1	LPCVD SiN	Deposite SiN on both sides with a 400 µm D-SOI substrate	Si, SiN	0.6 µm SiN
2	Photolithography #1	Pattern bottom side by Photoresist	AZ4330	3 µm AZ4330
3	RIE SiN	Pattern bottom side SiN by RIE	Si, SiN	0.6 µm SiN
4	Form bottom side cavity	Etch through from bottom side to D-SOI thin film by TMAH anisotropic etching	Si	8 hours 400 µm Si
5	Remove SiN and SiO2 on bottom	Remove SiN on bottom side and SiO2 of bottom SOI layer by RIE	SiO2, SiN	200 W CF_4/O_2
6	Photolithography #2	Pattern top side by Photoresist	AZ4330	3 µm AZ4330
7	Pattern SiN layer	Pattern SiN top layer by RIE	D-SOI, SiN	0.6 µm SiN
8	Apply photoresist	Apply photoresist on bottom to protect from HF	PR AZ4330	100°C, 5min
9	D-RIE Si etching #1	Etch through the Si on top SOI layer by D-RIE	D-SOI, Si	5 µm Si
10	HF wet Etching	Remove SiO2 on top SOI layer and form 2 µm undercut by HF wet etching	SiO2	2 µm SiO2
11	D-RIE Si etching #2	Etch through the Si on bottom SOI layer by D-RIE	D-SOI, Si	5 µm Si
12	Clean Photoresist	Clean AZ4330 with acetone and O_2 plasma	Acetone	200W, 20min
13	Remove SiN on top	Remove SiN top layer by Phosphoric acid	SiN	0.6 µm SiN
14	E-beam Evaporation Pt/Ti deposit	Deposit Pt/Ti on both side	Pt, Si	0.2 µm Pt
15	LPCVD parylene	Coating 20 µm parylene on top side	Parylene, Si	10 g Parylene
16	Pattern parylene	Pattern parylene for RIE	PR AZ 4620	15 µm
17	Parylene RIE etching	RIE parylene	Parylene	20 µm
18	Wafer Bonding	Bonding two wafers on parylene coated layer	Parylene	230°C, 1000N, 30min

A.3 Micro-Fabrication Process for 3D printing based MET Accelerometer

Step	Process Name	Description	Material	Parameters
1	LPCVD SiN	Deposite SiN on both sides with a 400 µm D-SOI substrate	Si, SiN	0.6 µm SiN
2	Photolithography #1	Pattern top side by Photoresist for lift-off	AZ4330	3 µm AZ4330
3	E-beam Evaporation Pt/Ti deposit	Deposit Pt/Ti on both side	Pt, Si	0.2 µm Pt
4	Lift-off	Lift-off electrodes	Acetone	8 hours
5	Stereolithography	Photosensitive polymer-like material for packaging tube	3D printing, Si	Room temperature
6	Assembling	Assemble MET element with 3D printed tube package by Epoxy	Epoxy	60 ºC, 8hours

A.4 Fabrication Process for 3D printing based Battery Accelerometer

Step	Process Name	Description	Material	Parameters
1	Mechanical Drilling #1	Mechanical drilling on 100 µm thick Copper Plate	Copper	100 µm Cu
2	Mechanical Drilling #2	Mechanical drilling on 100 µm thick Zinc Plate	Zinc	100 µm Zn
3	Stereolithography	Photosensitive polymer-like material for packaging tube	3D printing	Room temperature
4	Assembling	Assemble drilled Cu/Zn plate with 3D printed tube package by Epoxy	Epoxy	60 ºC, 8hours

BIOGRAPHICAL SKETCH

Mengbing Liang is currently in his 4th year of study in Electrical Engineering Ph.D. program at Arizona State University. He is a highly adaptable, detail-oriented Electrical Engineering Ph.D. candidate who has 4+ years of research experience in development of MEMS motion sensing system, semiconductor fabrication process, mixed-signal circuits design, signal process and space exploration (harsh environment).